Accepted Manuscript

A hydrodynamic stress model for simulating turbulence/particle interactions with immersed boundary methods

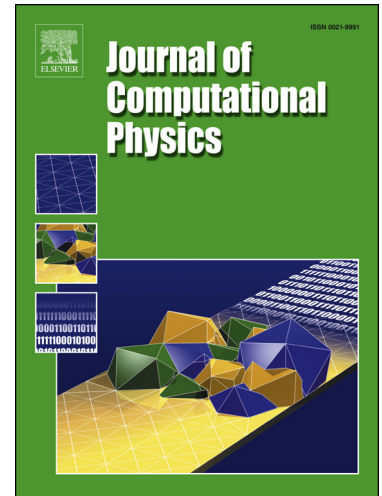Shizhao Wang, Marcos Vanella, Elias Balaras

Please cite this article in press as: S. Wang et al., A hydrodynamic stress model for simulating turbulence/particle interactions with immersed boundary methods, *J. Comput. Phys.* (2019), https://doi.org/10.1016/j.jcp.2019.01.010

Highlights

- A model that accurately reconstructs the forces on an immersed body is proposed.
- It is based on the boundary layer (BL) equations and accounts the effects of surface curvature.
- The model requires numerical resolution that places 1 to 2 points in the boundary layer around the particle.
- It is applicable to simulations of turbulence interacting with particles of arbitrary shape.
- Several 2D and 3D benchmark flows are in excellent agreement with reference data.

A hydrodynamic stress model for simulating turbulence/particle interactions with immersed boundary methods

Shizhao Wang[b], Marcos Vanella[a], Elias Balaras[a,1]

[a]*Department of Mechanical and Aerospace Engineering, The George Washington University*
[b]*LNM, Institute of Mechanics, Chinese Academy of Sciences*

Abstract

In this work we propose a hydrodynamic stress model that accurately reconstructs the forces on an immersed body, with application to the simulation of turbulence interacting with finite-size particles of arbitrary shape. The proposed model is local and is based on the boundary layer approximation, where the effects of surface curvature on the pressure variation are accounted for. Numerical experiments show that the model requires about one or two grid points within the boundary layer to accurately reconstruct the hydrodynamic force distribution. This reduces significantly the cost of resolving the flow field around the particles. The accuracy of the proposed model is evaluated in a variety of flows with increasing complexity. In particular, results for the flows over stationary and oscillating circular cylinders, free falling cylinders and spheres, and the interaction of turbulence with spheres and ellipsoids will be presented.

Keywords: hydrodynamic stress model, immersed boundary method, particle-resolved direct numerical simulations

1. Introduction

Understanding the physics of turbulence-particle interactions is of great importance in a variety of problems in science and engineering, such as fluidization in chemical reactors, cloud formation in the atmosphere, pollutant transport in the oceans, drug delivery in the human body, and so forth [1, 2, 3, 4]. Numerical simulations have greatly enhanced our understanding of such complex physics and can be classified into two broad categories: point-particle models which are appropriate when the particle size is smaller than the Kolmogorov length scale at dilute concentrations [5, 6, 7]; finite-size particle approaches where the flow around around the particles is resolved. Several numerical schemes have been proposed for this task, including the arbitrary Lagrangian-Eulerian (ALE) method [8], Lattice Boltzmann methods (LBM) [9, 10, 11], fictitious-domain methods [12, 13, 14, 15, 16], and immersed boundary (IB) methods [17, 18, 19, 20, 21]. The latter has the advantage of being easily integrated into existing Navier-Stokes solvers on structured grids, and efficiently dealing with moving boundaries without the need for re-meshing [22]. In most IB formulations the effect of the solid body on the flow is represented by a volume force term (referred to as *IB forcing term*) in the momentum equations, which can be implemented in different ways (see [23] for a review).

Uhlmann [19] proposed a formulation, directly targeting particulate flows, where the Navier-Stokes equations are solved on a Cartesian grid, and the particle's surface is defined by a set of Lagrangian control points. The force density is evaluated at the Lagrangian points using a kinematic constraint, and then transferred to the Eulerian mesh via transfer kernels. These kernels are designed to ensure momentum conservation, while the *total* hydrodynamic force acting on the particle can be directly evaluated from the IB force and the inertia force due to artificial flows within the particle [19]. This greatly simplifies the computation of hydrodynamic forces, when compared to direct integration of the friction and pressure forces acting on the surface of the particle. Several variants of this method have been proposed, and focus primarily on improving the approximation of the non-slip condition on the particle surface and the computation of the hydrodynamic forces [24, 25, 26, 21, 27, 28]. Example applications using this class of methods include isotropic turbulence interacting with up to 6400 spherical particles [29], channel flow turbulence

---

[1]Corresponding author: balaras@gwu.edu.

interacting with thousands of spherical particles [30, 31], and turbulent open channel flow with bed-load sediment transport [32, 33, 34].

A common trait of the above efforts is that they all involve rigid spherical particles, primarily because the application of this methodology to non-spherical and/or flexible particles is not straightforward, even when the particulate flows are dilute enough to ignore contact forces between solids. This is due to the challenges associated with accurate computation of the local hydrodynamic surface stresses, as well as, the large expense incurred in tracking and identifying an arbitrarily shaped solid in space. The location of the center of mass, orientation, and possibly a displacement field with respect to an equilibrium configuration are needed to fully describe the solid motion, in contrast to the center point location and diameter required for rigid spherical particles. As a result a substantial increase in computational cost is incurred. Some of the above methods cannot be directly extended to flows involving non-spherical particles as they are formulated to produce only integral hydrodynamic forces [19].

Local hydrodynamic forces can be evaluated from the local flow information. This requires the boundary layer around the particles to be resolved, imposing very fine grid requirements (see the details in Section 4.2). In practice, however, despite the fact that the grid sizes utilized for particulate turbulence are usually much larger than those used for the corresponding single phase turbulence, the boundary layers around particles are not properly captured and the accurate estimation of the hydrodynamic forces is a challenge [35, 36]. The primary aim of this work is to address this challenge and provide an accurate and cost efficient formulation to estimate the distribution of hydrodynamic forces on coarse grids for particles of arbitrary shapes. We focus on the dilute particles of the order of Taylor-length scale where the boundary layer around the particles is laminar. Our strategy is to engage a model, which is inspired by the two-layer model utilized in large-eddy simulations [37], to estimate the quantities that cannot be resolved by the grid. The proposed hydrodynamic stress model takes into account the effect of the particle surface curvature on the flow, and is applicable to particles of arbitrary shape.

The rest of the manuscript is organized as follows. The problem description and basic solver are provided in Section 2. The proposed scheme to compute hydrodynamic stresses on coarse meshes is outlined in Section 3. Validation of the method on a range of problems of increasing complexity, and parallel performance of our implementation are reported in Section 4. Finally, a summary and conclusions are given in Section 5.

2. Problem formulation and numerical method

2.1. Fluid motion and immersed boundaries

The fluid motion is modeled by the Navier-Stokes equations for incompressible flows in a inertial frame, $\mathcal{N}$,

$$\frac{\partial \mathbf{u}}{\partial t} + \nabla \cdot (\mathbf{u} \otimes \mathbf{u}) = -\nabla p + \frac{1}{Re} \nabla^2 \mathbf{u} + \mathbf{f}, \tag{1a}$$

$$\nabla \cdot \mathbf{u} = 0, \tag{1b}$$

where $\mathbf{u}$ is the non-dimensional velocity, p is the non-dimensional pressure, t is non-dimensional time. The characteristic length, velocity, density, time, and force to get the non-dimensional variables are L, U, ρ_f, L/U, and $\rho_f(UL)^2$, respectively, where ρ_f is the density of fluid. The Reynolds number is defined as, $Re = UL/\nu$, where ν is the kinematic viscosity of fluid. The vector $\mathbf{f}$ represents external forces applied on the fluid. In the discrete equations, $\mathbf{f}$, contains the IB forcing term. In this work, Eq. (1a)-(1b) are solved using an explicit, pressure correction, fractional step method [38]. A standard, second-order, central-difference discretization on a staggered grid is used for the spatial derivatives and an explicit, second-order Adams-Bashforth scheme is used for time integration. To advance the solution from time t^{k-1} to $t^k = t^{k-1} + \Delta t$, compute:

$$\tilde{\mathbf{u}} = \mathbf{u}^{k-1} + \frac{\Delta t}{2} \left(3\mathbf{H}(\mathbf{u}^{k-1}) - \mathbf{H}(\mathbf{u}^{k-2}) \right) - \Delta t \mathbf{G}(p^{k-1}) + \Delta t \mathbf{f}^{k-1/2}, \tag{2}$$

where $\mathbf{H}$ is a discrete operator containing the convective and viscous terms, $\mathbf{G}$ is a discrete gradient operator. $\mathbf{f}^{k-1/2}$ is the IB forcing term discussed below. The pressure correction δp is calculated based on $\tilde{\mathbf{u}}$:

$$\mathbf{L}\delta p = \frac{1}{\Delta t} \mathbf{D}\tilde{\mathbf{u}}, \tag{3}$$

2

where **L** and **D** are discrete Laplacian operator and divergence operator, respectively. Finally, the velocity and pressure at time step k are given by:

$$\mathbf{u}^k = \tilde{\mathbf{u}} - \Delta t \mathbf{G}\delta p \quad , \quad p^k = p^{k-1} + \delta p. \tag{4}$$

The direct, Lagrangian forcing scheme based on moving least squares (MLS) transfer functions proposed in [25], is used to compute the IB forcing term. Nevertheless, any IB interpolation method in the literature can be potentially used on the following derivations. First, the predicted velocity $\mathbf{u}^*$ that doesn't take into account internal boundaries is computed by:

$$\mathbf{u}^* = \mathbf{u}^{k-1} + \frac{\Delta t}{2}\left(3\mathbf{H}(\mathbf{u}^{k-1}) - \mathbf{H}(\mathbf{u}^{k-2})\right) - \Delta t \mathbf{G}(p^{k-1}). \tag{5}$$

Then, the predicted velocity is evaluated on all Lagrangian points on the surface of the particles, as illustrated in Figure 1a. In particular the predicted velocity, $\mathbf{U}_m^*$, at the mth Lagrangian marker is interpolated from $\mathbf{u}^*$ as follows:

$$\mathbf{U}_m^* = \sum_{i=1}^{ne} \phi_i^m(\mathbf{x}_i)\mathbf{u}_i^*, \tag{6}$$

where ne is the number of Eulerian points in the support domain associated to m. $\phi_i^m(\mathbf{x}_i)$ is an interpolation function relating the Lagrangian marker, m, with each member of its support domain. Here we use MLS interpolation to define $\phi_i^m(\mathbf{x}_i)$ [25, 39]. The IB forcing term at the mth Lagrangian point $\mathbf{F}_m^{k-1/2}$ is computed by:

$$\mathbf{F}_m^{k-1/2} = \frac{\mathbf{U}_m^b - \mathbf{U}_m^*}{\Delta t}, \tag{7}$$

where $\mathbf{U}_m^b$ is the velocity of the boundary at the mth Lagrangian point. The IB forcing term is then transferred at the Eulerian grid points, i, as follows:

$$\mathbf{f}_i^{k-1/2} = \sum_{m=1}^{nl} c_m \phi_i^m(\mathbf{X}_m)\mathbf{F}_m^{k-1/2}, \tag{8}$$

where nl is the number of Lagrangian points. ϕ_i^m is the same shape function in Eq. (6). $\mathbf{X}_m$ is the position of the mth Lagrangian point. c_m is the ratio between the volume associated the mth Lagrangian point (as the ΔV_m shown in figure 1a) and the averaged Eulerian grid volume. Conservation of total force and torque acting on the fluid is ensured by this transfer operation (see [25] for details).

2.2. Particle motion

In this section the equations inherent to arbitrary rigid body motion in three dimensional space are described. Two reference frames are used to describe motion of particles of arbitrary shape as shown in Figure 1b. The motion of the center of mass of each particle is described in the inertial frame, $\mathcal{N}$. Besides, $\mathcal{N}$, each particle has a body-fixed frame, $\mathcal{B}$, attached to the center of mass to define its geometry and orientation.

The motion of rigid particles is governed by the Newton-Euler equations. For the Sth particle, we have:

$$\mathbf{M}_S \frac{d\mathbf{V}_N^S}{dt} = \mathbf{F}_{N,h}^S + \mathbf{F}_{N,e}^S, \tag{9a}$$

$$\mathbf{I}_S \frac{d\mathbf{\Omega}_N^S}{dt} = \mathbf{Mt}_{N,h}^S + \mathbf{Mt}_{N,e}^S, \tag{9b}$$

where the subscript N indicates that the vector is expressed in terms of the basis unit vectors of the inertial frame $\mathcal{N}$. $\mathbf{M}_S$ and $\mathbf{I}_S$ are the mass matrix and inertia matrix of the Sth particle, $\mathbf{V}_N^S$ and $\mathbf{\Omega}_N^S$ are the linear and angular velocity of the mass center of the Sth particle, respectively. $\mathbf{F}_{N,h}^S$ and $\mathbf{Mt}_{N,h}^S$ are the hydrodynamic force and moment acting on the Sth particle, respectively. $\mathbf{F}_{N,e}^S$ and $\mathbf{Mt}_{N,e}^S$ are the force and moment acting on the Sth particle contributed by the external forces excluding hydrodynamic forces. The calculation of $\mathbf{F}_{N,h}^S$ and $\mathbf{Mt}_{N,h}^S$ for each particle will be discussed in Section 3.
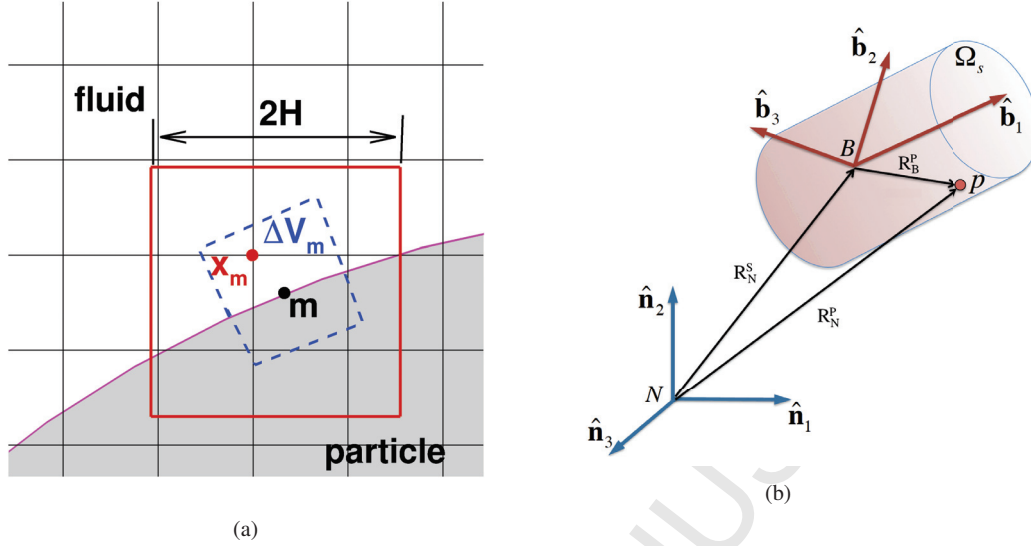
3

(a)

(b)

Figure 1: (a) Schematic of the supporting domain for a Lagrangian point. m is the Lagrangian point on the particle surface. x_m is the closest Eulerian grid point on which either pressure or velocity is defined. The supporting domain for Lagrangian point m is shown by a (red online) square (cubic in 3D grid) of $2H$ around m, where $H = 1.2h$ and h is the Eulerian grid length. The volume ΔV_m associated with point m is shown by the (blue online) dashed line. (b) Schematic of global frame and body-fixed local frame.

Eqs. (9a) and (9b) for a set of rigid bodies $s = 1, 2, 3, \cdots, n$ can be rewritten in the general form:

$$\begin{bmatrix} \mathbf{I} & 0 \\ 0 & \mathbf{M} \end{bmatrix} \frac{d}{dt} \begin{pmatrix} \mathbf{q_1} \\ \mathbf{q_2} \end{pmatrix} = \begin{pmatrix} \mathbf{q_2} \\ \mathbf{F} \end{pmatrix}, \tag{10}$$

where $\mathbf{q_1}$ is the generalized displacement vector of the rigid body system, $\mathbf{q_2} = d\mathbf{q_1}/dt$ is the generalized velocity, $\mathbf{I}$ is the identity matrix, $\mathbf{M}$ is the generalized mass matrix, and $\mathbf{F}$ is the generalized forces vector. Details of the derivation of generalized displacement and velocities for each rigid body can be found in the Appendix.

Once the state of each particle is computed by solving Eq. (10), the kinematics of any point P on the S th particle is computed by:

$$\mathbf{R}_N^P = \mathbf{R}_N^S + [\mathbf{T}_{NB}]\mathbf{R}_B^P, \tag{11a}$$

$$\mathbf{V}_N^P = \mathbf{V}_N^S + \mathbf{\Omega}_N^S \times ([\mathbf{T}_{NB}]\mathbf{R}_B^P), \tag{11b}$$

$$\dot{\mathbf{V}}_N^P = \dot{\mathbf{V}}_N^S + \dot{\mathbf{\Omega}}_N^S \times \left([\mathbf{T}_{NB}]\mathbf{R}_B^P\right) + \mathbf{\Omega}_N^S \times \mathbf{\Omega}_N^S \times \left([\mathbf{T}_{NB}]\mathbf{R}_B^P\right), \tag{11c}$$

where $\mathbf{R}_N^P$, $\mathbf{V}_N^P$ and $\dot{\mathbf{V}}_N^P$ are the position, velocity, and acceleration of point P on the S th particle in the inertial reference frame $\mathcal{N}$. $\mathbf{R}_N^S$, $\mathbf{V}_N^S$, $\dot{\mathbf{V}}_N^S$ are the position, velocity and acceleration of the center of mass of the S th particle respectively. $\mathbf{R}_B^P$ is the position of point P in the body-fixed reference frame $\mathcal{B}$, and $\mathbf{\Omega}_N^S$ is the angular velocity of frame $\mathcal{B}$ respect to $\mathcal{N}$, in the inertial reference frame. Finally, $[\mathbf{T}_{NB}]$ is the orthogonal transformation matrix from body-fixed reference frame $\mathcal{B}$ to the inertial reference frame $\mathcal{N}$. To describe rotations in three dimensional space a set of Euler angles is used [40]. Details are given in the Appendix A. Both sets of equations for fluid and particles are integrated in time using a partitioned, predictor-corrector scheme [41]. The use of strong coupling, although more expensive, allows for the use of particle-fluid density ratios of unity or less.

3. Computing hydrodynamic stress on a coarse grid

Evaluation of the hydrodynamic stresses on particle-turbulence interaction simulations is a great challenge, because the grid around the particle is usually not fine enough to properly resolve the velocity gradients. Below we will review existing approaches in the context of particulate flows and outline the proposed model.

4

3.1. Limitations of available schemes

The momentum balance approach utilized in [19, 27, 21], evaluates the total hydrodynamic force by the sum of the IB forcing term and the fluid acceleration inside the solid body:

$$\mathbf{F}_{N,h} = -\int_V \mathbf{f}dV + \frac{d}{dt}\int_V \mathbf{u}dV, \tag{12a}$$

$$\mathbf{M}_{N,h} = -\int_V \mathbf{r}\times\mathbf{f}dV + \frac{d}{dt}\int_V \mathbf{r}\times\mathbf{u}dV, \tag{12b}$$

where $\mathbf{F}_{N,h}$ and $\mathbf{M}_{N,h}$ are the hydrodynamic force and moment, respectively. V is the volume occupied by the solid body on the Eulerian grid. $\mathbf{f}$ is the IB forcing term on the Eulerian grid, and $\mathbf{r}$ is the position vector with respect to the object's center of mass. The first term on the right side of Eqs. (12a)-(12b) is computed by adding the IB forcing term and its moment on the Lagrangian points, as the transfer functions between Eulerian and Lagrangian grids are designed to preserve the total force and moment. In spherical particle cases, the second term on the right-hand-side of Eq. (12a) can be approximated using the acceleration of the center of mass, $\dot{\mathbf{u}}_c$, and particle volume V_c [19], $\frac{d}{dt}\int_V \mathbf{u}dV \approx V_c\dot{\mathbf{u}}_c$, or evaluated numerically using the diameter of the sphere to identify the particle volume [19, 21].

For a particle of arbitrary shape, this method requires the identification the Eulerian cells within the domain occupied by the particle and the volume fraction of the boundary cells to correctly compute the integral. Moreover, the use of Eqs. (12a)-(12b) does not provide the distribution of hydrodynamic forces on the surface, and does not provide sufficient hydrodynamic force information in cases of deformable particles, or when statistics of the hydrodynamic surface stress are needed.

Alternatively the hydrodynamic forces can be computed by numerical integration of stresses along the body surface:

$$\mathbf{F}_{N,h} = \int_{\partial V} \tau\cdot\mathbf{n}dS, \tag{13a}$$

$$\mathbf{M}_{N,h} = \int_{\partial V} \mathbf{r}\times(\tau\cdot\mathbf{n})dS, \tag{13b}$$

where ∂V is the particle surface, $\mathbf{n}$ is the unit vector in the normal direction, and $\tau = -p\mathbf{I} + (\nabla\mathbf{u} + \nabla\mathbf{u}^T)/Re$ is the hydrodynamic stress tensor. This approach can provide both the total hydrodynamic forces and the distribution of the hydrodynamic stress acting on the particle surface. In [42] and [25] the surface hydrodynamic stresses are computed using a linear reconstruction along the normal direction (*normal probe*):

$$\begin{aligned}\tau|_m &= -p|_m\mathbf{I} + \frac{1}{Re}\left.(\nabla\mathbf{u} + \nabla\mathbf{u}^T)\right|_m,\\ &\approx -(p|_e + \left.\frac{D\mathbf{u}}{Dt}\right|_e \cdot\mathbf{n})\mathbf{I} + \frac{1}{Re}\left.(\nabla\mathbf{u} + \nabla\mathbf{u}^T)\right|_e,\end{aligned} \tag{14}$$

where the subscript e indicates the values at an external point e along the normal direction to the surface point m (see Figure 2). The shear stress at m is approximated by the one at the nearby external point e, implying a linear variation assumption for the velocity in the normal direction. Numerical experiments have demonstrated that this approach requires very fine grids to accurately resolve the velocity gradients within the boundary layer rendering it prohibitively expensive when applied to turbulent flows with finite-size particles.

Both the above methods should yield similar hydrodynamic forces if the grid is fine enough to resolve the particle boundary layers, which in most cases comes with a high computational cost. In Table 1 we summarize a few recent computations of particulate flows using IB methods and list the grid resolution utilized to resolve spherical particles, together with the particle Reynolds number, Re_p (based on the particle diameter and the convective velocity). It can be seen that in most cases the grid size is, $dh \simeq D/20$, which in the best case for the lower Re_p values, will place 2-3 grid nodes within the boundary layer (boundary layer thinkness, δ, is estimated from $\delta/D \sim 1/\sqrt{Re_p}$ [35]). With this resolution around a particle, approaches based on the numerical integration of stresses along the body's surface will under-predict the hydrodynamic forces.

5

Table 1: Grid length and Reynolds number for particle-resolved simulations. D is the diameter of the particle. dh is the grid length. Re_p is the Reynolds number based on the diameter of the particle and the convective or fluidization velocity.

Ref.	D/dh	Re_p	flow state
Uhlmann [19]	12.8	≈ 400	turbulent flow
Uhlmann [30]	12.8	136	turbulent flow
Botto and Prosperetti [36]	16	80	turbulent flow
Xu and Subramaniam [35]	20	50	turbulent flow
Pan et at. [43]	9.3	$O(1000)$	turbulent flow
Wachs [16]	10	29	-
Rahmani and Waches [44]	24	106 to 625	laminar flow
Uhlmann and Dusek [45]	15 to 48	185 to 365	laminar flow
Kempe and Frohlich [21]	up to 22	up to 200	laminar flow

3.2. Proposed hydrodynamic stress model

Let us limit our discussion to flows where the particle boundary layers are laminar, which covers a wide range of applications. In such case the flow can be approximated by the boundary layer equations in a local orthogonal curvilinear coordinate system. We start with two-dimension flows in the local coordinate system $\xi - \eta$ (see Figure 2):

$$\frac{\partial u_\xi}{\partial t} + \frac{u_\xi}{h_\xi}\frac{\partial u_\xi}{\partial \xi} + u_\eta \frac{\partial u_\xi}{\partial \eta} = -\frac{1}{h_\xi}\frac{\partial p}{\partial \xi} + \frac{1}{Re}\frac{\partial^2 u_\xi}{\partial \eta^2}, \tag{15a}$$

$$\frac{\partial h_\xi}{\partial \eta}u_\xi^2 = \frac{\partial p}{\partial \eta}, \tag{15b}$$

where p is the pressure, and u_ξ and u_η are velocity components in the streamwise (ξ) and normal (η) directions, respectively. Here, the rectilinear axis η is defined in the normal direction to the solid surface (into the fluid region). The curvilinear ξ is defined by the intersection between the plane spanned by η and the relative velocity of the fluid at the external point e with respect to point m, and the surface of the body. According to the axis definition, the scale factor h_η is 1 and h_ξ depends on the surface curvature. In contrast to flat-plate boundary layer flows, the momentum balance expressed by Eq. (15b), indicates that surface curvature generates a pressure gradient in the normal direction. Ideally, the local discretization and solution of Eqs. (15a)-(15b) can be employed to obtain the surface stresses [46, 37]. However, for particles of arbitrary shape and orientation with respect to the fluid grid, the implementation of such a scheme can be very complex leading to costly computations.

3.2.1. Evaluation of pressure on the particle surface

To avoid direct numerical solution of the above equations we can utilize Eq. (15b), which governs the pressure variation along the normal direction for the flow over a curvilinear boundary. The pressure gradient along a line $\xi = const.$ can be expressed in a general form:

$$\left.\frac{\partial p}{\partial \eta}\right|_{\xi=const.} = g(\eta), \tag{16}$$

where $g(\eta)$ is a function of normal coordinate η. The function $g(\eta)$ depends on the coupled effect of the surface curvature and the near flow field, and does not admit a universal expression. Assuming as a first order approximation that $g(\eta)$ varies linearly within the boundary layer, the pressure gradient and pressure near the particle surface are given by:

$$\frac{\partial p}{\partial \eta} = b_p + a_p\eta, \tag{17a}$$

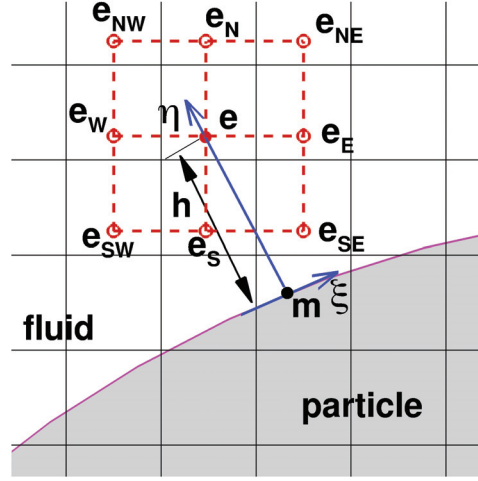$$p = c_p + b_p\eta + \frac{1}{2}a_p\eta^2, \tag{17b}$$

6

Figure 2: Schematic of the local curvilinear coordinate system and the external point arrary.

where a_p, b_p and c_p are coefficients to be determined by the local pressure information $p|_e$, $\partial p/\partial \eta|_e$, and $\partial p/\partial \eta|_m$. Here, $p|_e$ is the pressure at an external point e along the normal direction (as shown in Figure 2). $\partial p/\partial \eta|_m$ and $\partial p/\partial \eta|_e$ are the pressure gradient in the normal direction at the point m on the particle surface and the external point e, respectively.

The pressure at the external point e can be interpolated from the Eulerian grid. In this work the same interpolation technique used in computing the IB forcing term (i.e. Eq. 6) is employed:

$$p|_e = \sum_{i=1}^{ne} \phi_i^e p_i, \tag{18}$$

where ne is the number of Eulerian points in the supporting domain of external point e. Note that ϕ_i^e are the shape functions relating point e to its interpolation stencil. The pressure gradient in the normal direction at point m can be estimated by using the Navier-Stokes equations on the particle surface:

$$\left. \frac{\partial p}{\partial \eta} \right|_m = \left(-\frac{D\mathbf{u}}{Dt} + \frac{1}{Re}\nabla^2\mathbf{u} \right) \cdot \mathbf{n} \bigg|_m \approx -\frac{D\mathbf{u}}{Dt} \cdot \mathbf{n} \bigg|_m, \tag{19}$$

where $D\mathbf{u}/Dt$ is the material derivative of velocity and $\mathbf{n}$ is the unit normal vector at point m on the particle surface. The term $D\mathbf{u}/Dt$ at the particle surface is evaluated from the particle acceleration at m. The viscous force term $(1/Re)\nabla^2\mathbf{u}$ at the particle surface can be ignored, considering that it mainly contributes to the forces in the tangential direction. The computation of the pressure gradient $\partial p/\partial \eta$ at point e, defined in the curvilinear system $\xi - \eta$, is discussed below. Finally the pressure on the surface of the particle can be estimated by:

$$p|_m = p|_e - \frac{1}{2}\left(\left. \frac{\partial p}{\partial \eta} \right|_m + \left. \frac{\partial p}{\partial \eta} \right|_e \right) h, \tag{20}$$

where h is the distance between points m and e.

3.2.2. Evaluation of viscous stresses on the particle surface

The viscous stress on the surface of the particle can be evaluated using Eq. (15a), which can be simplified by ignoring the effect of inertia and convective terms as suggested by Posa and Balaras [46] and validated in Section 4.2

7

of this work. This simplification leads to the constraint that, in order to maintain accuracy, the first computational point off the wall should be positioned within the laminar boundary layer [46]. Eq. (15a) reduces to,

$$\frac{1}{Re} \frac{\partial^2 u_\xi}{\partial \eta^2} = \frac{1}{h_\xi} \frac{\partial p}{\partial \xi}. \tag{21}$$

The effect of curvature on the variation of $\partial p/\partial \xi$ in the normal direction can be investigated by taking the derivative $\partial/\partial \xi$ on Eq. (15b)

$$\frac{\partial}{\partial \eta} \left(\frac{\partial p}{\partial \xi} \right) = \frac{\partial}{\partial \xi} \left(\frac{\partial h_\xi}{\partial \eta} u_\xi^2 \right), \tag{22}$$

where the relation $\frac{\partial}{\partial \xi} \left(\frac{\partial p}{\partial \eta} \right) = \frac{\partial}{\partial \eta} \left(\frac{\partial p}{\partial \xi} \right)$ is used. It is seen from the last equation that the surface curvature causes a variation of $\partial p/\partial \xi$ along the normal direction. Similar to the pressure, the variation of pressure gradient $\partial p/\partial \xi$ depends on the coupled effect of curvature and the flow conditions within the boundary layer, not admitting a universal exact expression. The linear function, $\partial p/\partial \xi = b + a\eta$, can serve as a first order approximation for the variation of $\partial p/\partial \xi$ in the normal direction. In this scenario, Eq. (21) reduces to

$$\frac{1}{Re} \frac{\partial^2 u_\xi}{\partial \eta^2} = b + a\eta \tag{23}$$

where a and b are two coefficients to be determined by the local flow information.

Based on Eq. (23), an analytical expression for the velocity profile at $\xi = const.$ can be obtained

$$u_\xi(\eta) = d + c\eta + \frac{b}{2}\eta^2 + \frac{a}{6}\eta^3, \tag{24}$$

where again, the c, d coefficients must be determined from the flow state. We use the non-slip condition at the boundary point m and the flow information at the external local point e to dynamically compute these coefficients

$$a = \left. \frac{\partial^3 u_\xi}{\partial \eta^3} \right|_e, \tag{25a}$$

$$b = \left. \frac{\partial^2 u_\xi}{\partial \eta^2} \right|_e - \left. \frac{\partial^3 u_\xi}{\partial \eta^3} \right|_e h, \tag{25b}$$

$$c = \left. \frac{\partial u_\xi}{\partial \eta} \right|_e - \left. \frac{\partial^2 u_\xi}{\partial \eta^2} \right|_e h - \frac{1}{2} \left. \frac{\partial^3 u_\xi}{\partial \eta^3} \right|_e h^2, \tag{25c}$$

$$d = \left. u_\xi \right|_m. \tag{25d}$$

Finally, the viscous stress at point m on the particle surface can be given by

$$\begin{aligned} \mathbf{f}_\nu|_m &= \frac{1}{Re} \left. \frac{\partial u_\xi}{\partial \eta} \right|_m \mathbf{t} \\ &= \frac{1}{Re} \left. \frac{\partial u_\xi}{\partial \eta} \right|_e \mathbf{t} - \frac{1}{Re} \left. \frac{\partial^2 u_\xi}{\partial \eta^2} \right|_e h\mathbf{t} - \frac{1}{Re} \frac{1}{2} \left. \frac{\partial^3 u_\xi}{\partial \eta^3} \right|_e h^2 \mathbf{t}, \end{aligned} \tag{26}$$

where $\mathbf{t}$ is the unit vector in the tangent direction at point m.

The velocity and pressure gradients in Eqs. (25) and (20) at the external point e are defined in the $\xi - \eta$ system. The exact computation of these velocity gradients for a particle of arbitrary shape is not trivial. Therefore, an approximate

8

method is used to compute the velocity gradients at the external point e

$$\left.\frac{\partial p}{\partial \eta}\right|_e \approx \left.\frac{\partial p}{\partial x_i}\right|_e n_i, \tag{27a}$$

$$\left.\frac{\partial u_\xi}{\partial \eta}\right|_e \approx \left.\frac{\partial u'_i}{\partial x_j}\right|_e t_i n_j, \tag{27b}$$

$$\left.\frac{\partial^2 u_\xi}{\partial \eta^2}\right|_e \approx \left.\frac{\partial^2 u'_i}{\partial x_j \partial x_k}\right|_e t_i n_j n_k, \tag{27c}$$

$$\left.\frac{\partial^3 u_\xi}{\partial \eta^3}\right|_e \approx Re \left.\frac{\partial^2 p}{\partial x_i \partial x_j}\right|_e n_i n_j, \tag{27d}$$

where the subscript i, j, and k are the indices of the tensor, and the Einstein summation convention is applied. $\mathbf{n} = n_i \hat{\mathbf{n}}_i$ is the versor in the normal direction at point m, where $\hat{\mathbf{n}}_i$ ($i = 1, 2, 3$) are the coordinate unit vectors in $\mathcal{N}$. $\mathbf{t} = t_i \hat{\mathbf{n}}_i$ is the versor in the tangent direction at point m. The simplified Eq. (21) for a flat-plate, $1/Re\ \partial^2 u_\xi/\partial \eta^2 = \partial p/\partial \xi$, is used to approximate the 3rd order tangential velocity derivatives by, $\partial^3 u_\xi/\partial \eta^3 = Re\ \partial^2 p/\partial \xi \partial \eta$. This approximation was found to have little effect on the hydrodynamic forces in all the cases of this work. The derivatives $\partial u'_i/\partial x_j$, $\partial^2 u'_i/(\partial x_j \partial x_k)$, $\partial p/\partial x_i$ and $\partial^2 p/(\partial x_i \partial x_j)$ at the external point e is computed by the central difference scheme on an 3×3 points array (as shown in figure 2) for 2D flows and $3 \times 3 \times 3$ points array for 3D flows, centered at point e. The distance between neighbor points equals to the Eulerian grid length. The pressure on the points array is computed by using Eq. (18) for each point. The velocity u' at each point in the local coordinate array is computed by:

$$\mathbf{u}'\big|_E = \sum_{l=1}^{ne} \phi_l^E \mathbf{u}_l - \mathbf{\Omega}_N^S \times \mathbf{r}_N^E, \tag{28}$$

where the superscript E can be any point in the array. ne is the number of Eulerian points in the supporting domain of external point E. ϕ_l^E refers to the corresponding shape function set, as defined in Eq. (6). $\mathbf{\Omega}_N^S$ is the angular velocity of the Sth particle, where the Sth particle is the host of the marker m. $\mathbf{r}_N^E$ is the vector from the mass center of the Sth particle to external point E. The term $-\mathbf{\Omega}_N^S \times \mathbf{r}_N^E$ on the right-hand-side of Eq. (28) excludes the effect of rigid body rotation on the shear stress.

3.3. Discussion

The local acceleration and convection terms within the boundary layer are not taken into account in the model given by Eq. (23). Posa & Balaras [46] conducted *a priori* testing to investigate the effects of this assumption to the accuracy of two-layer models for laminar boundary layers, and found when the *modeled* boundary layer is captured with at least two grid nodes on the Eulerian grid the predicted wall stress is fairly accurate. If one ignores the pressure variation in the normal direction caused by curvature, the model given by Eq. (23) reduces to:

$$\frac{1}{Re} \frac{\partial^2 u_\xi}{\partial \eta^2} = b, \tag{29}$$

which is the Reduced Diffusion Model (RDM) proposed and proposed in [46]. In such case the analytical solution based on Eq. (29) has the form:

$$u_\xi(\eta) = d + c\eta + \frac{b}{2}\eta^2, \tag{30}$$

where the coefficients b, c, and d are determined as:

$$b = \left.\frac{\partial^2 u_\xi}{\partial \eta^2}\right|_e \quad , \quad c = \left.\frac{\partial u_\xi}{\partial \eta}\right|_e - \left.\frac{\partial^2 u_\xi}{\partial \eta^2}\right|_e h, \quad , \quad d = u_\xi\big|_m \tag{31}$$

and the corresponding viscous stress at point m on particle surface is given by:

$$\mathbf{f}_v|_m = \frac{1}{Re} \left.\frac{\partial u_\xi}{\partial \eta}\right|_e \mathbf{t} - \frac{1}{Re} \left.\frac{\partial^2 u_\xi}{\partial \eta^2}\right|_e h\mathbf{t}. \tag{32}$$

9

Eq. (32) contains only the first and second terms on the rhs of Eq. (26). Computing the viscous stress by using only the first term in Eq. (32), we arrive at the *normal probe* approach described in [42, 25]. In this sense, both the RDM and *normal probe* methods are special cases of the model proposed by this work.

In three-dimensional boundary layers, the curvilinear term of the momentum balance equation in the normal direction, Eq. 15, will be given by a more complex form involving the curvature in the direction normal to the $\xi - \eta$ plane. However, the pressure gradient within the boundary layer can still be modeled by the linear functions in Eqs. (17a) and (23). Thus, the proposed hydrodynamic stress model is applicable to both two- and three-dimensional boundary layers. We should also point out that no assumptions on the geometry of the particle are made, as for example with momentum balance approaches [19]. In this sense, the proposed model works for arbitrarily shaped, rigid or deformable particles. Potential limitations originate form the validity of the model assumptions locally, as well as grid resolution.

One aspect that was not discussed in the formulation above is the handling of particle-particle collisions, which are common in particulate flows. The current formulation could serve as the basis to develop physics-based models for collisions, but this task is beyond the scope of the proposed work. To address this issue we combine the current method with a collision model to account for the short-range interaction between the particles. We use the collision model proposed in [47] for simulations with spherical particles, where a tuned short range repulsive force is defined to avoid the overlapping of the particles. The repulsive force is computed as follows:

$$\mathbf{F}^p = \begin{cases} 0, & \text{for} \quad d > 2R + \Delta, \\ \frac{\delta \mathbf{X}}{\varepsilon_P}(2R - d)^2, & \text{for} \quad 2R < d \le 2R + \Delta, \\ \frac{\delta \mathbf{X}}{\varepsilon_P'}(2R - d), & \text{for} \quad d \le 2R. \end{cases} \tag{33}$$

where R is the radius of the particle, $\delta \mathbf{X} = \mathbf{X}_l - \mathbf{X}_t$ and $\delta \mathbf{X} = \mathbf{X}_t - \mathbf{X}_l$ are the distance vectors in computing the repulsive forces for the leading particle and the trailing particles, respectively, $\mathbf{X}_l$ and $\mathbf{X}_t$ are the position vectors of the mass center of the leading particle and trailing particle, respectively, d is the distance between the particle mass centers. $\Delta = 3dh$ is the range of the repulsive force, dh is the grid length of the Eulerian grid, $\varepsilon_P = 5 \times 10^{-7}$ and $\varepsilon_P' = \sqrt{\varepsilon_P}$ are small positive stiffness parameters for particle-particle collisions. For the interactions between the particles and the wall, the distance between the particles is replaced by the distance between a particle and the imaginary particle with respect to the wall.

4. Results

In this section we present a series of test problems of increasing complexity to demonstrate the accuracy and efficiency of the proposed hydrodynamic stress model. In the test problems, the geometric shape of particles admits an analytical expression, in order to use the the well documented benchmarks of these kind of flows. However, the proposed hydrodynamic stress model is applicable particles with arbitrary shape.

4.1. Flow over a stationary circular cylinder

Consider a circular cylinder of diameter D fixed in a uniform cross-flow with velocity U, at Reynolds number $Re = UD/\nu = 40$. The flow is steady and two-dimensional. The simulation is conducted on a computational domain of $[-10D, 20D] \times [-11D, 11D]$, where the center of the cylinder is at $(0, 0)$. The uniform upstream flow is specified at the inlet, and a convective boundary condition is used at the outlet. The free-slip boundary condition is set at the bottom and top boundaries. The non-slip boundary condition is enforced at the cylinder surface. The flow around a cylinder at this Reynolds separates and forms a steady 'dead-water' region, as shown in Figure 3. The separation point θ, geometrical measurements of the 'dead water' region (L, a and b as shown in Figure 3) and the drag coefficient, C_d, will be compared to reference data in the litersture. The scope of computations reported in this section is as follows: i) quantify the sensitivity to grid resolution of a typical immersed boundary approach, which utilizes the normal-probe to compute hydrodynamic forces; ii) evaluate the accuracy of the proposed model *a-priori*, utilizing a well resolved computation; iii) evaluate the accuracy of the proposed model *a-posteriori*, by comparison to reference results in the literature.
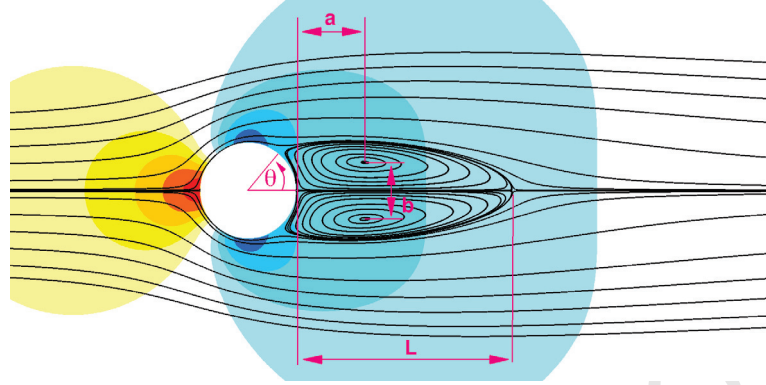
Figure 3: Pressure and streamlines around a stationary circular cylinder at Re = 40. The contours for pressure range from -0.5 (blue) to 0.5 (red) with 10 equal intervals.
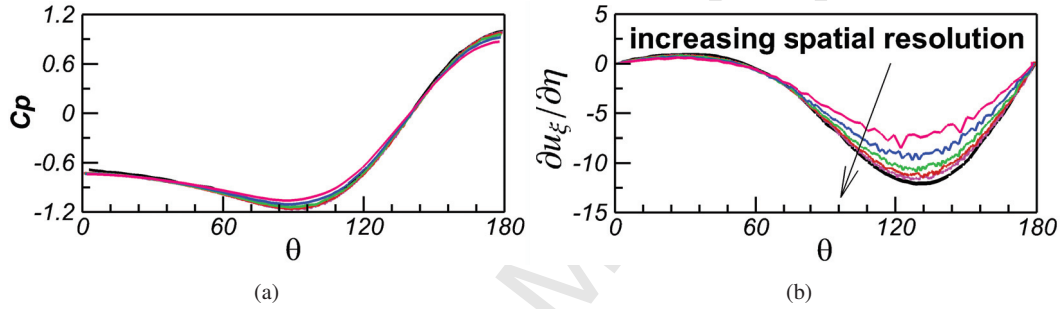

Figure 4: (a) Pressure coefficient, C_p; (b) velocity gradeint, $\partial u_\xi/\partial \eta$, on the cylinder's surface at Re = 40. The color lines shows the results computed by the *normal probe* approach based on different grid lengths. The grid lengths are $dh = D/24$, $dh = D/48$, $dh = D/96$, $dh = D/192$, and $dh = D/384$, respectively. The pressure coefficients are shifted by different constants for the simulations with different grids. The black line ———— shows the reference results by Braza *et al.* [49].

4.1.1. Sensitivity of hydrodynamic forces to grid resolution

To quantify the sensitivity of the hydrodynamic forces to grid resolution when computed using the *normal probe* approach for the MLS direct-forcing scheme discussed above we conducted a series of computations with increasing resolution. In each case the grid around the cylinder was approximately uniform and in the range of, $D/384 < dh < D/24$. The resulting distribution of pressure coefficient, C_p, and the tangential velocity gradient, $\partial u_\xi/\partial \eta$, on the cylinder's surface are shown in Figure 4. The pressure coefficient is fairly insensitive to the grid resolution, and all grids are within 2% of the reference solution. The tangential velocity gradient along the wall-normal direction, one the other hand, is clearly under-predicted on the coarser grids. To quantify the difference with the reference solution, we list the computed $\left|\partial u_\xi/\partial \eta\right|$ at $\theta = 130°$ on different grids (see Table 2). Approximately 192 grid points across the diameter of the cylinder are needed for the error to be less than 5%, while on the coarsest grid, $dh = D/24$, the error is 33.7%.

The prediction of the hydrodynamic force follows a similar trend. Table 2 also lists the drag force estimated by the *normal probe* approach for all grids. As expected the error in the viscous drag is higher than that on the pressure drag. For the coarsest grid ($dh = D/24$) these errors are 14.8% and 2% respectively. The grid resolution has to be increased at least 8 times (to $dh = D/192$) in each direction, to keep the errors within 5% when computing the viscous drag and within 2% in computing the total drag. These results are consistent with the findings of Tenneti et al. [48] on the convergence of hydrodynamic forces in IB methods.

We should also note that the errors in the computation of the hydrodynamics forces utilizing a *normal probe* approach depend on the details of the IB formulation as well as the position of the probe. In the present Lagrangian,

11

Table 2: Sensitivity of the tangential velocity gradient and drag force estimated with the *normal probe* approach for the flow around a circular at *Re* = 40. DT: total drag; DP: pressure drag; DV: viscous drag. The reference results are computed from Braza *et al.* [49] and the *difference* for a variable, ϕ, is defined as $(\phi_{comp} - \phi_{ref})/\phi_{ref} \times 100\%$

Grid length	$\|\partial u_\xi/\partial \eta\|$	diff %	DT	diff %	DP	diff %	DV	diff %
$D/24$	7.98	33.7%	0.73	−6.4%	0.50	−2.0%	0.23	−14.8%
$D/48$	9.57	20.6%	0.75	−3.8%	0.50	−2.0%	0.25	−7.4%
$D/96$	10.59	12.1%	0.76	−2.6%	0.50	−2.0%	0.25	−7.4%
$D/192$	11.45	4.9%	0.77	−1.3%	0.51	0.0%	0.26	−3.7%
$D/384$	11.82	1.9%	0.78	0.0%	0.51	0.0%	0.27	0.0%
Ref [49]	12.05	–	0.78	–	0.51	–	0.27	–

direct-forcing, MLS based IB approach the kernel width of 2.4*dh* and the probe extends 2.0*dh* from the wall. We find this configuration to have optimal cost/accuracy properties. For implementations with wider or narrower support domains and/or the use of higher order interpolations the force convergence may be different. Nonliner fittings or interpolations might help to improve the prediction to the wall shear stress in the *normal probe* approach. For the spherical particles, for example, spherical hamonic expansions may also give more accurate predictions. The proposed model, which is practically equivalent to a physics-based correction on the forces predicted by the *normal probe* approach, should be applicable to most direct-forcing, immersed boundary methods in a straightforward manner. Depending on the support domains for the transfer functions of the specific formulation, however, the location of the external point, *e*, as well as the grid resolution may have to be adjusted.

4.1.2. A-priori testing of the proposed model

To test the accuracy of model and examine its sensitivity to the location of the external point, *e*, (see Figure 2) in an idealized setting, we conducted *a-priori* testing using the solution on the grid with resolution, $dh = D/384$ as reference. Three cases were considered, where the external point, *e*, was located $2 \times D/96 \approx 0.02D$, $2 \times D/48 \approx 0.04D$ and $2 \times D/24 \approx 0.08D$ from the wall. The velocity and pressure at point, *e*, in each case was interpolated form the fine grid ($dh = D/384$) and was the input to the model. The resulting distribution of the pressure and tangential velocity near the wall are shown in Figure 5, where the corresponding profiles form the high resolution computation are included for comparison. In particular, three locations are shown with $\theta = 60°, 54°, 45°$ (see Figure 3 for the definition of θ). The locations were selected be around the separation point ($\theta = 54°$), after the separation point ($\theta = 45°$), and before the separation point at $\theta = 60°$, respectively. The reference solution on the fine grid ($dh = D/384$) shows that the pressure varies along the normal direction as implied by Eq. (15b), indicating that the surface curvature generates a non-zero pressure gradient in the normal direction near the wall.

For the case corresponding to a computation with the highest resolution ($dh = D/96$), where point, *e*, is located at $2 \times D/96 \approx 0.02D$ from the wall, the resulting pressure distribution is in good agreement with the reference solution at all locations. In addition, the pressure profiles satisfy the constrains that the pressure gradient is zero on the wall ($u_\xi = 0$ in Eq. 15b) and non-zero away from the wall ($u_\xi \neq 0$ and $\partial h_\xi/\partial \eta \neq 0$ in Eq. 15b). The prediction on the coarser grid (*e* is located $2 \times D/48 \approx 0.04D$ from the wall) is also good at all locations. When the external point is moved further away to $2 \times D/24 \approx 0.08D$, the pressure profiles still give a zero-pressure gradient near the wall and non-zero pressure gradient at the external point *e*, but the pressure is over-predicted in the region $0.5 < r < 0.54$ (the error is within 3%). This result is still better, however, from the assumption of a the constant pressure (or zero pressure gradient) near the wall. The tangential velocity profiles are also shown in Figure 5 for all three cases. The tangential velocity provided by the model (Eq. 24), captures the main features of the near wall flow even in the separated regime.

We also conducted a series of tests, where the location of the external point, *e*, was set to a fixed distance from the wall ($h = 2 \times D/24$), while the interpolation stencils to obtain the coefficients in Eq. (25) for example, corresponded to grids with increasing resolution and up to $D/192$. The resulting coefficients were always within 2% of the ones on the reference grid, indicating that interpolation errors play a lesser role in the accuracy of the model.
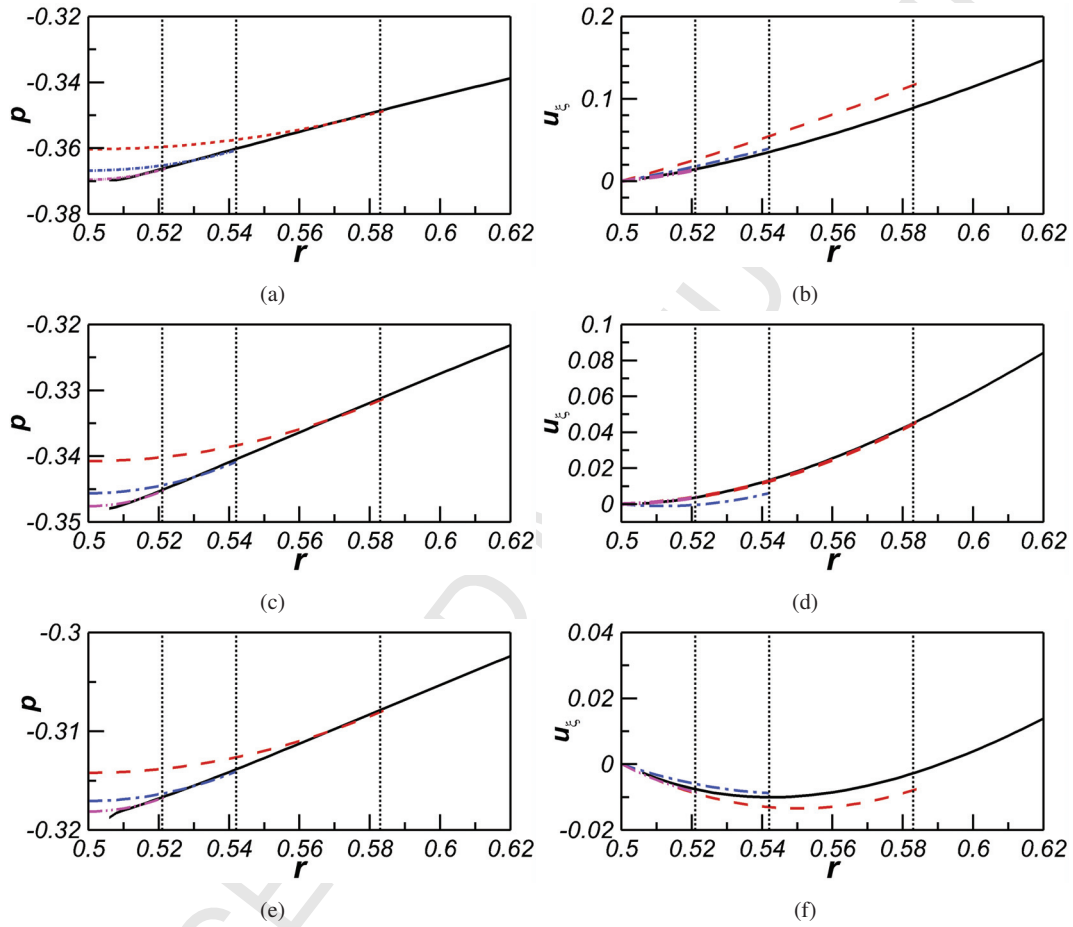
12

Figure 5: A-apriori testing of the proposed model for the case of the flow around a circular cylinder at Re=40 with varing grid resolution. Left column: presure profile along the wall-normal direction; Right column: tangential velocity profile along the wall-normal direction. (a,b) $\theta = 60°$; (c,d) $\theta = 54°$; (e,f) $\theta = 45°$. The grid resolution was: $dh = D/24$ $(---)$; $dh = D/48$ $(; -\cdot-)$; $dh = D/96$ $(-\cdot\cdot-)$. The external point, e was located at $2dh$ from the wall for each case and is indicated by the corresponging vertical dotted lines. The reference profiles are taken from the simulation with $dh = D/384$ $(\underline{\quad\quad})$.
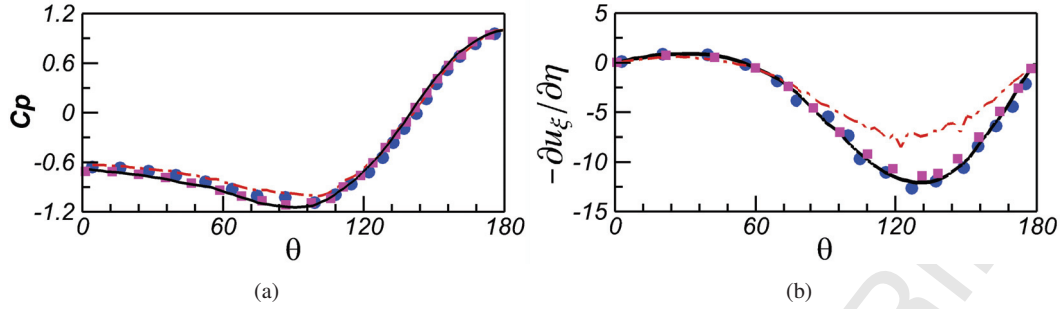
13

Figure 6: (a) Pressure coefficient, C_p; (b) velocity gradeint, $-\partial u_\xi/\partial \eta$, on the cylinder's surface at $Re = 40$. ———— Reference results by Braza *et al.* [49]; ● Proposed model on h=D/24; The *normal probe* approach on different grids: —·— $dh = D/24$; ■ $dh = D/192$
.

Table 3: Wake and drag coefficient of the flow over a stationary cylinder at, $Re = 40$, and grid resolution, $dh = D/24$.

Case	L/D	a/D	b/D	θ	C_d
Present	2.32	0.76	0.6	54.1°	1.55
Wang and Zhang [27]	2.36	0.72	0.6	53.8°	1.54
Coutanceau and Bouard [50]	2.13	0.76	0.59	53.8°	-
Linnick and Fasel [51]	2.28	0.72	0.6	53.6°	1.54
Taira and Colonius [52]	2.33	0.72	0.6	53.7°	1.54

4.1.3. A-posteriori testing of the proposed model

Finally here we will compare a computation utilizing the proposed model on the coarsest of the grids considered above ($dh = D/24$) to a computation without the model, as well as, to reference results in the literature. Figure 6 shows the predicted pressure and shear stress distribution on the cylinder's surface with and without utilizing the proposed model. The reference results by Braza *et al.* [49] where a boundary-conforming solver is used are also included for comparison. It can be seen that the pressure distribution is predicted fairly accurately by both schemes and is less sensitive to grid resolution. The wall stress is captured accurately by the proposed method, and is under-predicted when the model is switched-off. The predicted separation point, geometrical measurements of the 'dead water' region, L, a and b (as defined in Figure 3) and the drag coefficient, C_d, are listed in Table 3 in comparison to reference data in the litersture. All quantities are in excellent agreement with the literature despite the coarse grid resolution. The error in the drag coefficient for example, is less that 2%. As we discussed above, to reduce the error to this level with the *normal probe* approach a grid with spacing less than $dh = D/384$ (16 times finer in each direction) is required.

To better understand the near-wall behaviour of the model, the pressure and velocity fields obtained with the proposed model on $dh = D/24$ are compared to a high resolution computation on very fine grid with $dh = D/384$. Isolines of the pressure and velocity distribution in the vicinity of the cylinder are shown in Figure 7. The coarse grid solution consists of two parts: the outer flow computed on the Eulerian grid with $dh = D/24$, and the near wall flow predicted by the model. The *boundary* between the two is indicted by the dashed line in the figure. The agreement is very good and consistent with the *a-priori* testing we reported in the previous section. A detailed quantitative comparison of pressure and velocity profiles near the wall is shown in Figure 8. As with the above figure, inner (predicted by the model) and outer (computed on the $dh = D/24$ grid) profiles are compared to the reference computation with $dh = D/384$. The velocity profiles (see Figure 8b) are in excellent agreement with the reference solution in both zones. The pressure profiles agree well with the reference solution in the outer part (see Figure 8a). Good agreement can be also be observed in most locations at the inner part, with the largest errors in area of the adverse pressure gradient before separation.
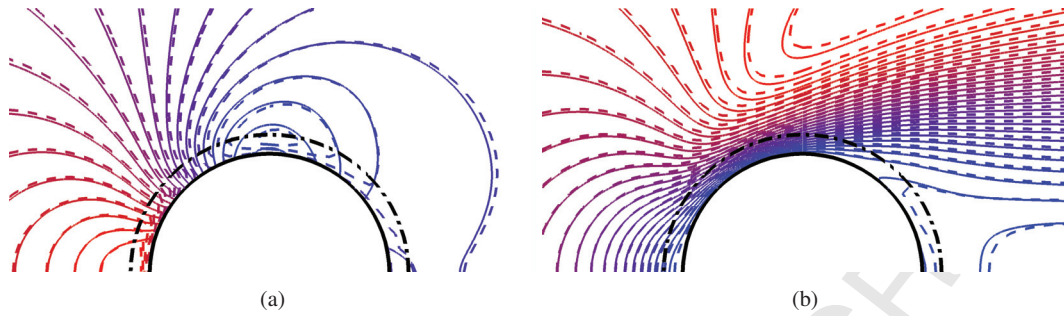
14

(a)   (b)

Figure 7: Flow around a circular cylinder at $Re = 40$. (a) Iso-contours of the pressure (range: 0.5 red to -0.5 blue, with an equal interval of 0.05); (b) Iso-contours of the streamwise velocity (range 1.15 red to -0.1 blue with an equal interval of 0.05). $-\cdot-$ coarse grid computation ($dh = D/24$) with the proposed model; ——— fine grid ($dh = D/384$) computation. The dash-dotted circle indicates the position of the external point e, at $D/12$ from the wall.
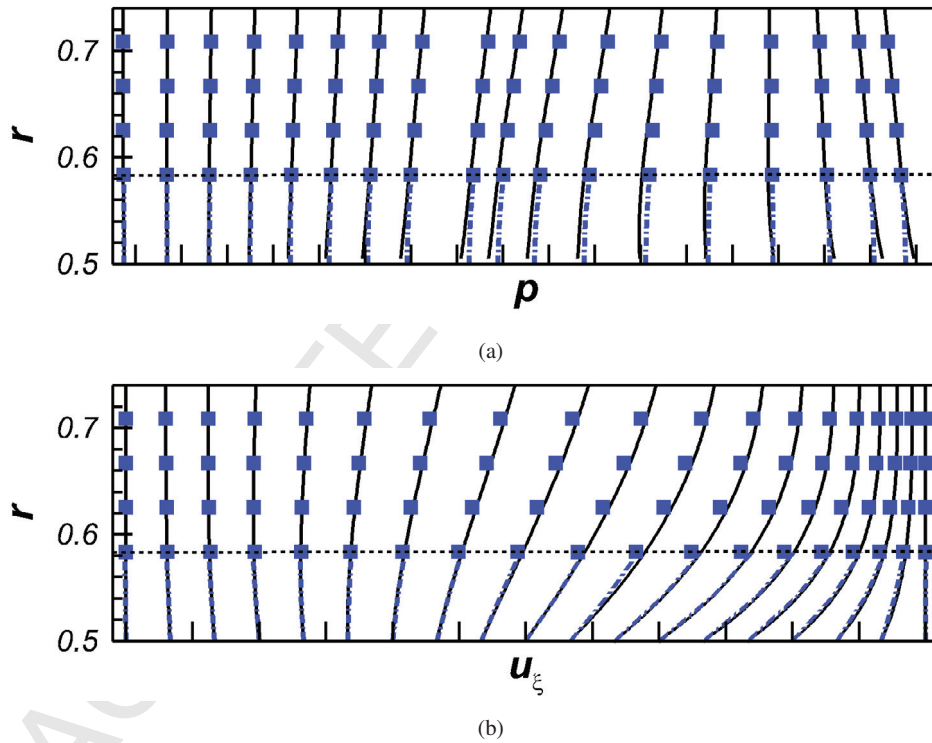

(a)

(b)

Figure 8: Flow around a cylinder at Re=40. (a) pressure profiles along the wall-normal direction, (b) tangential velocity profiles along the wall-normal direction. The profiles are shifted by different constants along the horizontal axis to avoid overlapping with each other. The 19 lines from left to right correspond to the angle from $\theta = 0^o$ to $\theta = 180^o$ with equal interval of 10°. The spaces between the ticks on the horizontal axis for the pressure and the tangential velocity are 0.2 and 0.5, respectively. ——— reference computation at $dh = D/384$; $-\cdot-$ near wall profile predicted by the proposed model; ■ outer velocity profile at $dh = D/24$. The external point, e, was located at $D/12$ from the wall as inidicated by the horizontal dotted lines.
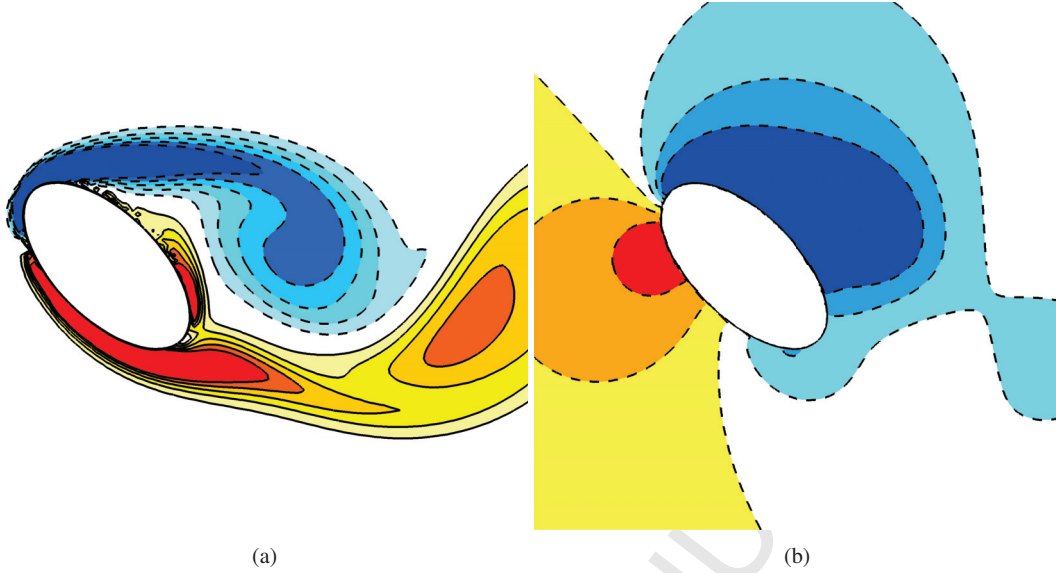
15

Figure 9: Instantaneous vorticity and pressure around an elliptical cylinder with $Re = 200$ at $t = 6.0$, (a) vorticity, from -5 (blue) to 5 (red), 10 intervals, (b) pressure, from -1.6 (blue) to -0.6 (red), 5 intervals.

4.2. Unsteady flow over a stationary elliptical cylinder

An elliptical cylinder with aspect ratio of $b/a = 2.0$, where a and b are the minor and major axes, respectively, is considered. The object is fixed and is subject to a cross-flow with an angle of attack (AoA) of $45°$. The Reynolds number is $Re = Ub/\nu = 200$, where U and ν are the magnitude of freestream velocity and kinematic viscosity of the fluid rerspectively. The computational domain is $[-25a, 25a] \times [-25a, 25a]$ and the body is located at the center. A uniform velocity, U, is specified at the inlet, and a convective condition is used at the outlet. Free-slip boundary condition is applied at bottom and top boundaries. A uniform Cartesian grid with cell size, $dh = a/24$, is used. The cylinder surface is represented by 128 uniformly distributed Lagrangian points.

For this Reynolds number the flow around the ellipse is unsteady. Pairs of vortices are shed from the leading and trailing edge alternatively as shown in Figure 9. In Figure 10 the hydrodynamic forces acting on the body are plotted in the form of the drag, $C_d = F_x/(0.5\rho U^2 b)$, and lift, $C_l = F_y/(0.5\rho U^2 b)$, coefficients ($F_y$, F_x are the drag and lift forces acting on the elliptical cylinder). At the lower part of the figure the evolution of the corresponding percentage error when compared to the reference solution at a grid $dh = a/192$, is also plotted. It is clear that, at this grid size, the *normal probe* approach under-predicts these forces when compared to the reference simulation. The maximum error in the lift coefficients are about 16% of the time-averaged lift coeffcients, while the error of lift coefficient predicted by using the proposed model is within 4%. The errors on the drag coefficeint are smaller in magnidute, but still the proposed model performs much better with a maximum error less than 2%. Similar trends can be seen in the distribution of the pressure coefficient and boundary vorticity on the surface of the body, shown in Figure 11. Overall the hydrodynamic stress model proposed provides remarkably accurate hydrodynamic total and distributed forces on the same grid as compared to reference data.

4.3. Unsteady flow over an oscillating circular cylinder

In this case the proposed hydrodynamic model is tested on a canonical flow with a moving boundary. It consists of a circular cylinder oscillating transversely in an uniform upstream flow. The oscillation is prescribed by,

$$y(t) = A \, cos(2\pi f_e t), \tag{34}$$

where $y(t)$ is the time-dependent transverse position of the cylinder center, A is the oscillating amplitude, f_e is the excitation frequency, and t is time. The Reynolds number based on the inflow velocity U and cylinder diameter D is
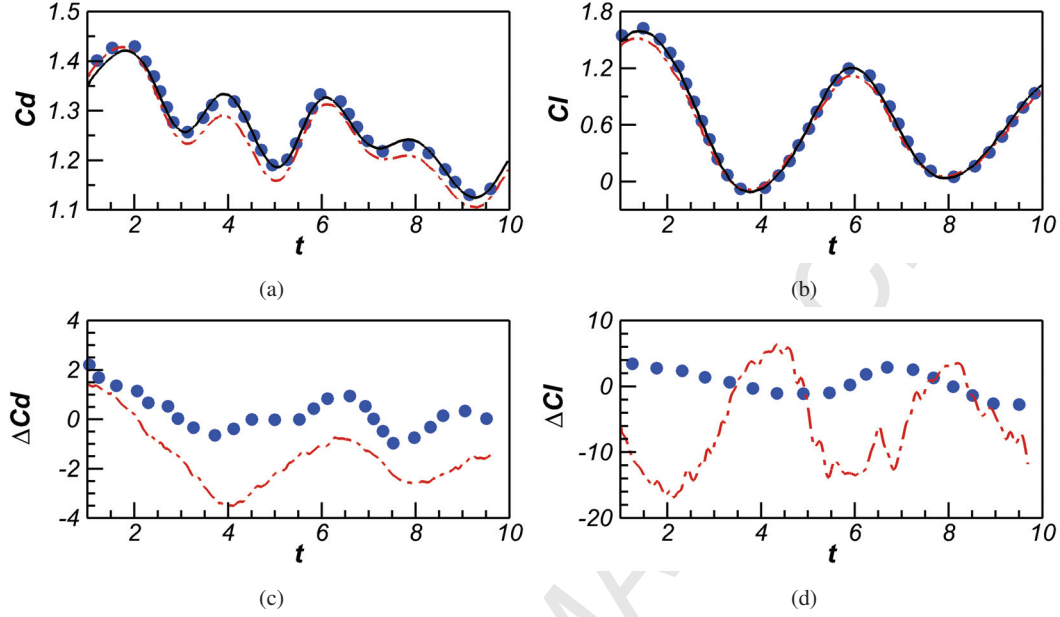
(a)

(b)

(c)

(d)

Figure 10: Drag and lift coefficients of an elliptical cylinder as a function of time, ● present model, − · − *normal probe* approach, and ─── reference simulation on a fine grid with $dh = a/192$. (a) drag coefficient; (b) lift coefficient; (c) and (d) is the corresponding percentage difference form the reference solution defined as $\Delta Cd = |Cd - Cd_{ref}|/\langle Cd_{ref}\rangle \times 100$ and $\Delta Cl = |Cl - Cl_{ref}|/\langle Cl_{ref}\rangle \times 100$, where $\langle Cd_{ref}\rangle$ and $\langle Cl_{ref}\rangle$ are the averaged drag and lift coefficients during $1 \leq t \leq 10$.
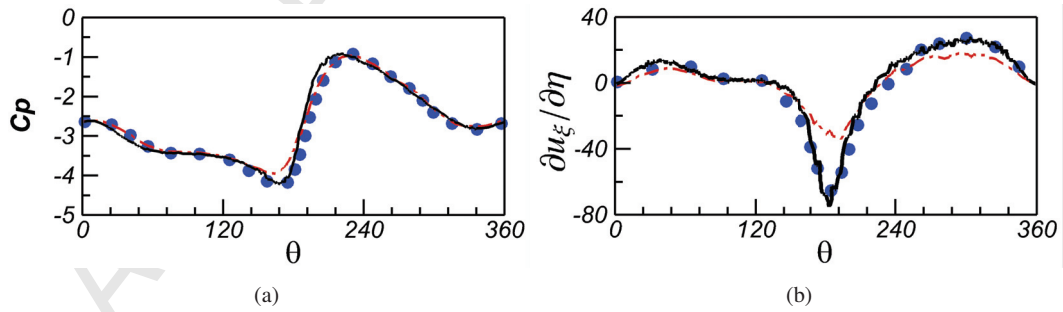

(a)

(b)

Figure 11: Distribution of pressure and vorticity around the elliptical cylinder at $Re = 200$ on the coarse grid with $dl = a/24$, ● present model, − · − *normal probe* approach, and ─── reference, (a) pressure coefficient, (b) vorticity. The reference is the simulation on a fine grid with $dh = a/192$.
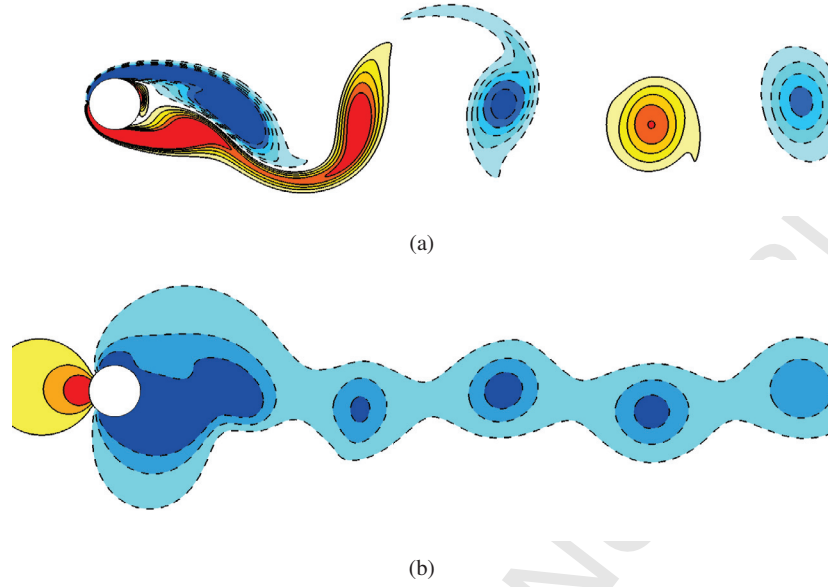
17

(a)

(b)

Figure 12: Instantaneous flow field of the transversely oscillating cylinder with the excitation frequency f_e/f_0 = 0.8 and Re = 185, (a) vorticity, from -2 (blue) to 2 (red), 10 intervals, (b) pressure, from -0.3 (blue) to 0.3 (red), 6 intervals.

$Re = UD/\nu$ = 185. The oscillating amplitude is A/D = 0.2. The excitation frequency is f_e/f_0 = 0.8, where f_0 = 0.195 is the natural vortex shedding frequency of a stationary circular cylinder at Re = 185.

The non-dimensional computational domain is $[-10, 40] \times [-15, 15]$, where the characteristic length is D. Identical boundary conditions as in the two previous cases are prescribed in the domain. The uniform grid size is set to a coarse value $dh = D/24$, and 128 uniformly distributed Lagrangian markers are mapped on the cylinder surface. The flow over the cylinder is unsteady, and a pair of vortices is shed in each oscillating period. The vorticity and pressure field at the time level when the cylinder reaches the maximum vertical position are shown in figure 12. The distribution of pressure coefficient and boundary vorticity at the same time are shown in figure 13. As shown in the previous cases, while the *normal probe* approach under-predicts the viscous stress (represented by boundary vorticity) on coarse meshes, the hydrodynamic stress model proposed correctly predicts the distribution of hydrodynamics forces on the same grids. The reference data are taken from the work of Guilmineau and Queutey [53], where the simulation is conducted on a boundary-conformal mesh with the first points of the mesh in the fluid locating at $dh = 0.001D$ away from the wall. The simulation based on the IB method with the *normal probe* approach needs to use a grid size of
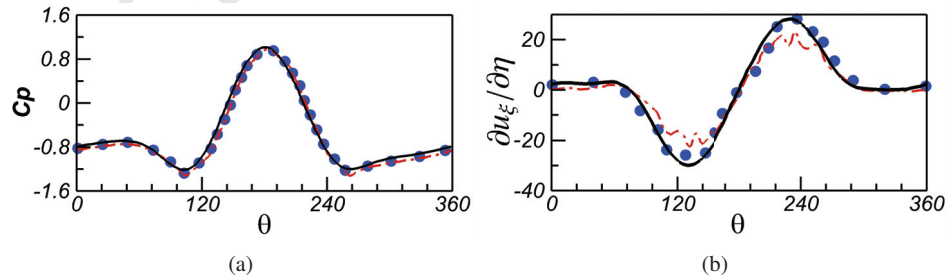

(a)   (b)

Figure 13: Distribution of pressure coefficient and vorticity around the cylinder at the instant when the vertical position of the cylinder reaches maximum, f_e/f_0 = 0.8, Re = 185, ● present model, – · – *normal probe* approach, and ——— reference, (a) pressure coefficient, (b) vorticity. The reference data are taken from the reference [53].

18

Table 4: Setup parameters for free falling sphere test cases

Case	ρ_s/ρ_f	$U_t/(m/s)$	$Re = U_t D/\nu$	gD/U_t^2
I	1.16	0.091	11.6	17.75
II	1.17	0.128	31.9	8.97

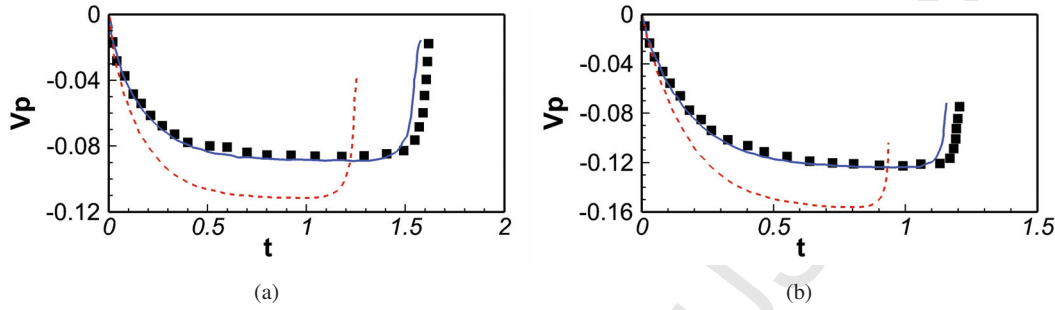(a)   (b)

Figure 14: Sedimentation velocity as function of time for a falling sphere at different Reynolds numbers, ——— present model, −− *normal probe* approach, and ■ reference, (a) $Re = U_t D/\nu$ = 11.6, (b) $Re = U_t D/\nu$ = 31.9. v_p is the dimensional sedimentation velocity, with a unit of m/s. t is the dimensional time, with a unit of second. The reference results are from [54]

$dh = D/250$ to get the correct distribution of vorticity on the cylinder surface [25].

4.4. Free falling sphere

In this case, the motion of a free falling sphere due to gravity in a initially stationary flow is simulated, to test the proposed model in a three-dimensional fluid-structure interaction problem. The simulation is set up according to the landmark experimental work in [54]. The experiments are carried out in a box filled with silicon oil. The dimensions of the box are $100mm \times 100mm \times 160mm$ along the depth, width and height directions, respectively. The distance between the sphere center and the box bottom is $127.5mm$, and it is released with a zero velocity. The terminal Reynolds number ranges from 11.6 to 31.9. The resolution around the sphere was set to $dh = D/24$ for all cases considered. The density ratios ρ_s/ρ_f, the measured sedimentation velocity U_t, non-dimensional gravity gD/U_t^2, and Reynolds numbers based on terminal velocity $Re = U_t D/\nu$ for the two cases considered in this study are listed in Table 4.

In Figure 14 the sedimentation velocities as a function of time are shown for both cases we considered. As the sphere moves downward under the influence of gravity it accelerates, and after some time, the weight is balanced by the hydrodynamic force. From that point and on the sphere moves with a constant terminal velocity. The predicted sedimentation velocities with the proposed model are in excellent agreement with the experimental results. The *normal probe* approach, on this coarse grid, over-predicts the sedimentation velocity by approximately 30% in higher Reynolds number case. The typical flow field just after the terminal velocity has been reached, is shown in Figure 15.

4.5. The drafting-kissing-tumbling of two 2D circular cylinders

To investigate the accuracy of the model in cases with particle-particle interactions we considered the case of drafting-kissing-tumbling of a pair of circular cylinders. The setup and parametric space were selected to much the computations reported by Uhlmann [19]. The details are given in Table 5. The pair of circular cylinders with identical diameters and density, are released in a container with fluid at rest, as shown in Figure 16(a). The initial vertical and horizontal offsets between the cylinders are 2D and 0.002D, respectively. The initial velocity of the fluid is zero. The no-slip boundaries conditions are used on all boundaries. The gravity is along the vertical direction (*x*-axis). The computational domain is discretized with a uniform grid mesh of $dh = D/24$. Each cylinder is discretized with 128 Lagrangian points. When the cylinders are released they cylinders *sink* due to the gravity. The interactions between
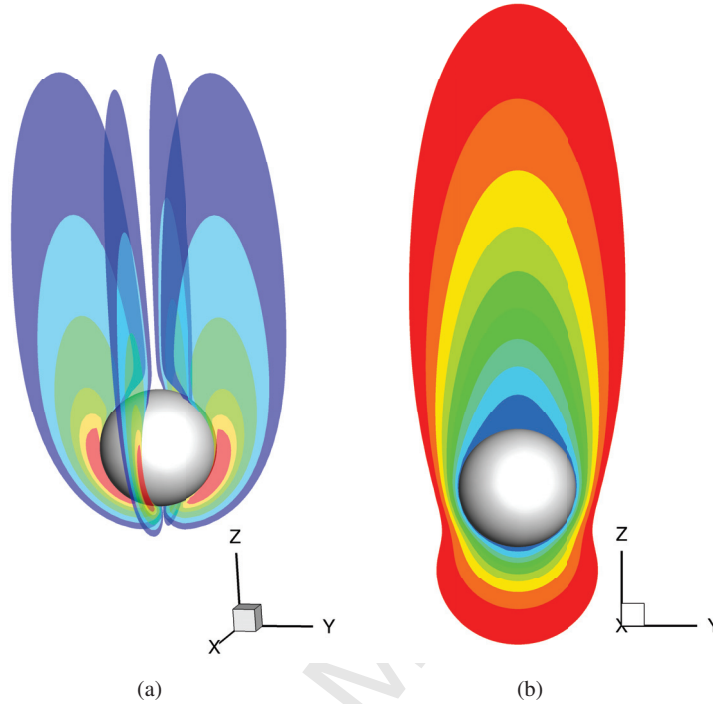
19

Figure 15: Instantaneous flow field around the free falling sphere at $Re = 31.9$, (a) vorticity magnitude, from 0.5 to 4.0, 7 intervals, (b) vertical velocity in the plane of $x = 0$, from -1 to -0.2, 8 intervals.

the leading and trailing cylinders involve a thin gap between the cylinders. Short-range hydrodynamic, solid-solid interaction (lubrication correction), and solid-solid contact models are needed when the gap between the cylinders is less than the Eulerian grid length. We use a repulsive force model proposed by Wan and Turek [47] to account for the direct interaction between the cylinders. We conducted two computations: one with the proposed model, and one where the hydrodynamic forces are computed using the *normal-probe* approach.

Three snapshots in time from each case are compared in Figure 16, where the distribution of the vorticity and the position of the cylinders is shown. The trailing cylinder stays in the wake of the leading cylinder in the early stage, as shown in Figure 16(b,e). The wake of the leading cylinder reduces the drag acting on the trailing cylinder, causing the speedup of the trailing cylinder, which catches up (see Figure 16c,f). The direct interaction between the cylinders results in a lateral motion and tumbling, as shown in Figure 16(d,g). The cylinder trajectories for the computations with and without the proposed model are very different. A quantitative comparison of the sedimentation velocities of the leading and trailing cylinder is shown in Figure 17. The reference experiments in [43] and the computations by [19] are added for comparison. The simulations without the model over-predict the sedimentation velocity, especially the sedimentation of the leading cylinder, which results in late cylinder-cylinder interactions. The proposed model reproduces the experimental results fairly accurately.

4.6. Turbulence interacting with finite-size particles

To demonstrate efficiency of the proposed approach in challenging configurations we considered the interaction of forced isotropic turbulence with spheres and ellipsoids. Forced isotropic turbulence is generated in a domain with dimensions, $[-\pi, \pi] \times [-\pi, \pi] \times [-\pi, \pi]$, using the linear forcing method proposed in [55], where the source term, $\mathbf{f_{iso}} = a_0(k_0/k)\mathbf{u}'$, ($a_0$ is a parameter to determine the input energy, k_0 is the desired steady state turbulent kinetic

Table 5: Setup parameters for the drafting-kissing-tumbling of two 2D cylinders

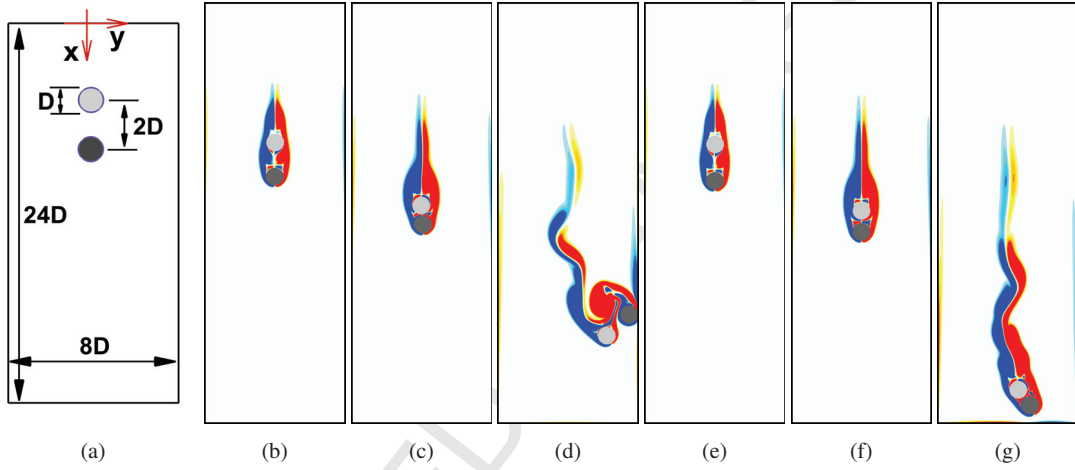|	
Diameter	0.25
Density	1.5
Gravity	981
Fluid viscosity	0.01
Domain size	$[0, 6] \times [-1, 1]$
Initial locations	$(1, 0.001), (1.5, -0.001)$

(a) (b) (c) (d) (e) (f) (g)

Figure 16: The simulations of drafting-kissing-tumbling of two 2D cylinders, (a) schematic of the initial arrangement, (b)-(d) vorticity around the cylinders in the simulations with the proposed model at $t = 1.2$, 1.7, and 2.9, respectively, (e)-(g) vorticity around the cylinders in the simulations without the proposed model at $t = 1.2$, 1.7, and 2.9, respectively. The contours for vorticity range from -50 (blue) to 50 (red). The dark grey and light grey cylinder are initially the leading and trialing cylinders, respectively.
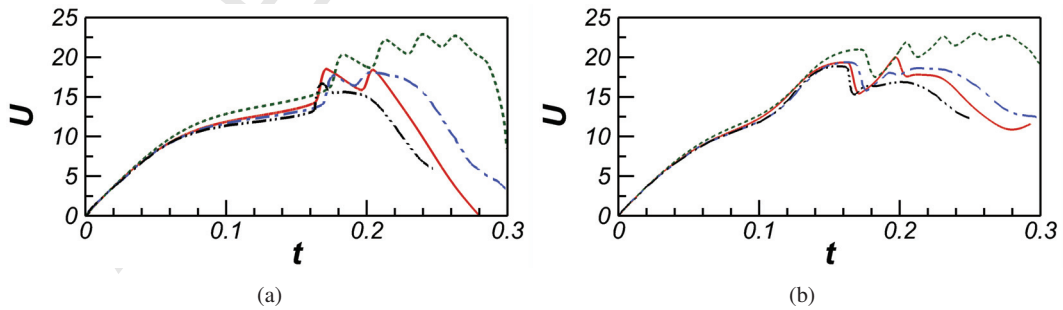

(a) (b)

Figure 17: The sedimentation velocities of the (a) leading- and (b) trailing-cylinders, respectively. ——— present model, $- - -$ *normal probe* approach, $- \cdot \cdot -$ reference computation [19], and $- \cdot -$ reference experiment [43].

21

energy, k is the instantaneous turbulent kinetic energy, and $\mathbf{u'}$ is the fluctuating of velocity) is introduced in the *rhs* of the momentum equation.

The spherical particles have a diameter of $D = \pi/8$, while ellipsoidal particles have a major-axis of $a = \pi/4$, and two minor-axes of $b = c = \pi/8$. For both cases the density ratio between the particles and the fluid is 1.02. For both cases we considered a volume fraction of 0.2%. The contact model by Wan and Turek [47] is used to avoid the overlap among particles, although in a dilute system like the one at hand, contact among particles does not happen often. The simulations are conducted on a grid of $256 \times 256 \times 256$. The time step is $dt = 3.0 \times 10^{-4}$ consistent with numerical stability and physical time-scales. The coefficients for the forcing function, $\mathbf{f_{iso}}$ are set to, $a_0 = 0.96$, $k_0 = 17$, and the resulting Reynolds number of $Re_\lambda = 116$. The integral length scale is $L = 3.35$, and the large eddy turn over time is $T = 0.96$.

Typical flow structures are shown in Figure 18, where the particles are larger than the Kolmogorov scale. The shear flows generated near the surface of the particles are visible. These shear flows may reduce velocity fluctuations by increasing the energy dissipation. At the same time, the wakes produced the by the particles enhance the production of the turbulent kinematic energy and increase the velocity fluctuations [56]. The effects of the particle type on turbulence can be quantified by computing the probability density function (p.d.f.) of the velocity fluctuations (see Figure 19a). The p.d.f. of u, for example, can be computed as follows [57]:

$$p(u_i) = \frac{1}{\delta u} \frac{N_i}{N_p}, \tag{35}$$

where, u_i is the ith value of a set of equally spaced values from u_{min} to u_{max}. The velocity interval between two consecutive values is $\delta u = (u_{max} - u_{min})/100$ and N_i is the number of grid points with $u_i - \delta u/2 < u_p \leqslant u_i + \delta u/2$. The probability density functions for the other velocity components, v and w, are calculated in similar manner. We sampled 100 realizations over a time period of $240 \leqslant t < 390$, resulting in $N_p = 100 \times 256 \times 256 \times 256$. The extreme velocity events are damped by the particles, especially the spherical particles. The damping of the extreme velocity events can be clearly seen in in Figure 19a where the turbulence fluctuations with spherical particles decay faster when $\xi > 3$. The ellipsoidal particles generate more energetic wakes than the spherical particles and as a result the velocity fluctuations decrease with a lower rate.

The p.d.f.s of the angular velocity of the particles is an important quantity in characterizing this complex interaction and are shown in Figure 19b. To compute this quantity, the rotational velocity of each particle is saved at each time step in the simulation. In this case the number of sample points, N_p, used to compute the p.d.f of rotational velocity is, $N_p = N_t \cdot n_p$, where n_p is the number of the particles ($n_p = 9$ for ellipsoids, and $n_p = 18$ for spheres), and N_t is the number of discrete time levels used in the sampling. The probability density function of Ω^2 is:

$$p((\Omega^2)_i) = \frac{1}{\delta(\Omega^2)} \frac{N_i}{N_p}, \tag{36}$$

where, $\Omega^2 = \mathbf{\Omega} \cdot \mathbf{\Omega}$ is the inner product of angular velocity. $(\Omega^2)_i$ is the ith component of the equally spaced values from $(\Omega^2)_{min}$ to $(\Omega^2)_{max}$. The velocity interval between two consequent values is $\delta(\Omega^2) = ((\Omega^2)_{max} - (\Omega^2)_{min})/100$ and N_i is the number of grid points with $(\Omega^2)_i - \delta(\Omega^2)/2 < (\Omega^2)_p \leqslant (\Omega^2)_i + \delta(\Omega^2)/2$. The resulting p.d.f. shown in Figure 19b uses $N_t \times N_P = (8.33 \times 10^5) \times 18$ points for spherical particles and $N_t \times N_P = (8.33 \times 10^5) \times 9$ points for ellipsoidal particles, where $N_t = 8.33 \times 10^5$ is within the simulation time interval of $250 < t < 500$ with $dt = 3.0 \times 10^{-4}$.

Both spherical and ellipsoidal particles show similar behavior when the angular velocity is low ($\Omega^{*2} < 5$). At higher rotation speeds ($\Omega^{*2} > 5$), the p.d.f of ellipsoidal particles takes lower values when compared to that of the spherical particles, likely due to the fact that ellipsoidal particles are less prone to rotation at the speeds defined in this particular problem setup. This is intuitively expected, given the same level of turbulent forcing on both sets of simulations, but higher rotational inertia of the ellipsoids. Another reason might be that the ellipsoidal particles tend to align preferentially with the principal axis of the fluid strain. Overall the effects of the particle types on turbulence, as demonstrated in by the statistics above, is consistent with the experimental observations by Bellani et al. [56], even through the current simulations are conducted at lower Reynolds numbers.

We have also conducted the simulations without the proposed model. There is no apparent difference on the p.d.f of the fluid phase, as shown in Figure 19(a). However, the rotation of the particles will be over-predicted because of the under-prediction of the shear stress if the proposed model is not used, as shown in figure 19(b). The differences

22

between the model and normal probe approach in the p.d.f of the velocity fluctuations is small, probably caused by the relatively low Reynolds number in the simulation. However, the p.d.f.s of the particle rotation speed are different and reflect a higher rate for the case of the normal probe approach. This is consistent with the trend by this approach to under-predict the shear stress on the particle surface. The detailed interactions between the turbulent statistics and the rotation of the particles at Reynolds numbers comparable to the experiments will be discussed in the subsequent work.

5. Summary and conclusions

The immersed boundary (IB) method is an efficient tool to investigate the interaction of turbulence with finite-size particles. Most of the particle resolved simulations of turbulence using IB formulations employ undeformable spherical particles and compute the total hydrodynamic force by using momentum balance considerations. The application of the momentum balance method to non-spherical and/or flexible particles is not straightforward, as it does not provide the distribution of hydrodynamic forces on the particle surface. The reconstruction of flow field near the particle surface can provide the distribution of the hydrodynamic forces but requires very fine grids to resolve the boundary layers, rendering the computations prohibitively expensive.

Inspired by the two-layer model in large-eddy simulation and its application in near-wall reconstruction for the IB method, in this work we propose a hydrodynamic stress model to estimate the hydrodynamic forces in under-resolved cases. The hydrodynamic model is based on the boundary layer equations and takes into account the effects of surface curvature on the flow field. The curvature effect is introduced as a factor that directly affects the variation of flow in the normal direction. By assuming a linear variation of pressure within the boundary layer, analytical expressions for pressure and velocity are given in a local curvilinear coordinate system. These polynomial function coefficients are computed dynamically by using local flow information. For accurate prediction of the hydrodynamic stress at any point on the particle surface, this model requires numerical resolution that places 1 to 2 points in the boundary layer. The proposed model is applicable to the cases where the particle boundary layer is laminar, which covers a wide range of the turbulent flows interacting with finite-size particles.

The proposed formulation also serve as the basis to develop, physics-based models for particle-particle collisions. This however, is a non-trivial task which is the focus of future work. Here the we coupled the current method with a collision model to account for the short-range interaction between the particles. We used the collision model proposed in [47] for simulations with spherical particles, where a tuned short range repulsive force is defined to avoid the overlapping of the particles.

Acknowledgements

Appendix A. Rigid body kinematics and dynamics

Appendix A.1. Kinematics

When dealing with multiple detached rigid bodies in a single inertial reference frame $\mathcal{N}$, it is convenient to derive their equations of motion in terms of this frame. In order to do this, both $\mathcal{N}$ and a body-fixed frame $\mathcal{B}$ are used to describe the motion, as shown in figure 1b. The coordinate of a point P on the Sth rigid body can be defined as

$$\mathbf{R}_N^P = \mathbf{R}_N^S + [\mathbf{T}_{NB}]\mathbf{R}_B^P, \tag{A.1}$$

where $\mathbf{R}_N^P$ is the coordinate vector of point P in the inertial frame $\mathcal{N}$, and $\mathbf{R}_B^P$ is the location of the point respect to the body's center of mass in terms of the body-fixed frame $\mathcal{B}$. All the vectors with subscript N in this work are expressed in the terms of unit vectors $\hat{\mathbf{n}}_1, \hat{\mathbf{n}}_2, \hat{\mathbf{n}}_3$ in the inertial frame $\mathcal{N}$, and all the vectors with subscript B are expressed in the terms of unit vectors $\hat{\mathbf{b}}_1, \hat{\mathbf{b}}_2, \hat{\mathbf{b}}_3$ in the body-fixed frame $\mathcal{B}$. $\mathbf{R}_N^S$ is the coordinate vector of the center of mass of the Sth
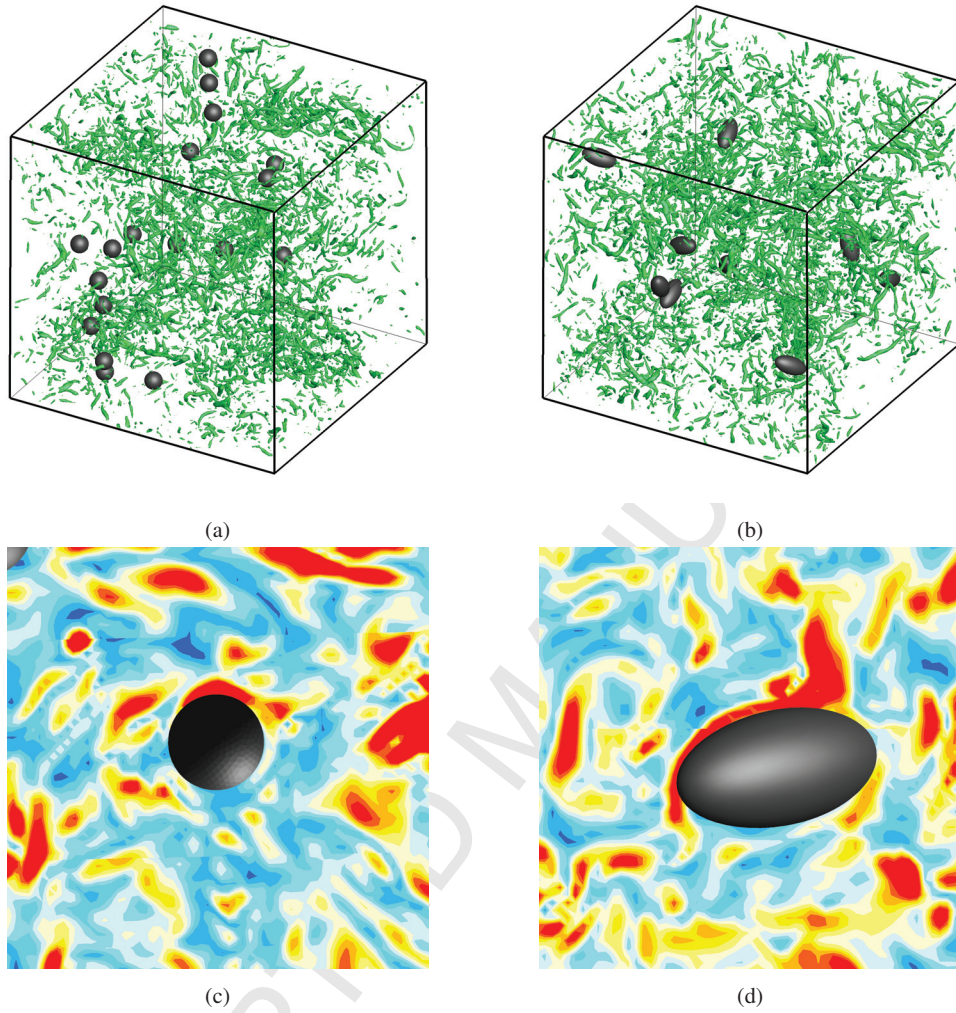
(a)

(b)

(c)

(d)

Figure 18: Particle-turbulence interaction, (a) vortex structures around spherical particles, (b) vortex structures around ellipsoidal particles, (c) vorticity magnitude around one spherical particle, from 0 (blue) to 100 (red), 10 intervals, (d) vorticity magnitude around one ellipsoidal particle, from 0 (blue) to 100 (red), 10 intervals.
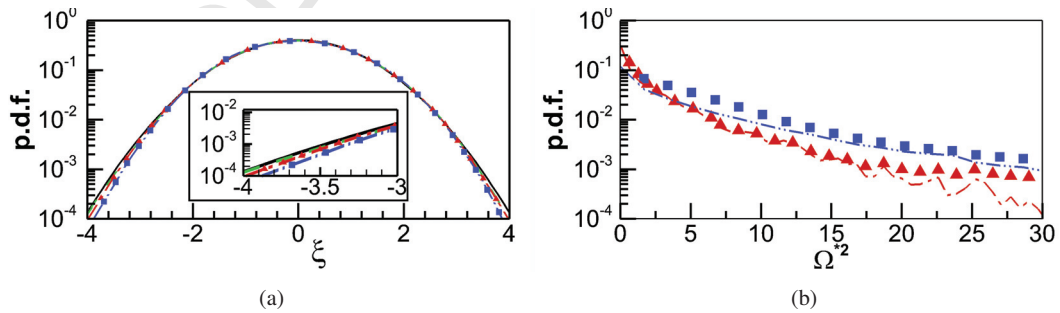

(a)

(b)

Figure 19: (a) The normalized probability density function of the turbulence with different particles. (b) The probability density function of the particle's rotating speed. ——— normal distribution, − − single phase, − · − ellipsoidal particles with model, − · ·− spherical particles with model, ▲ ellipsoidal particles, *normal probe* approach, ■ spherical particles with model, *normal probe* approach.
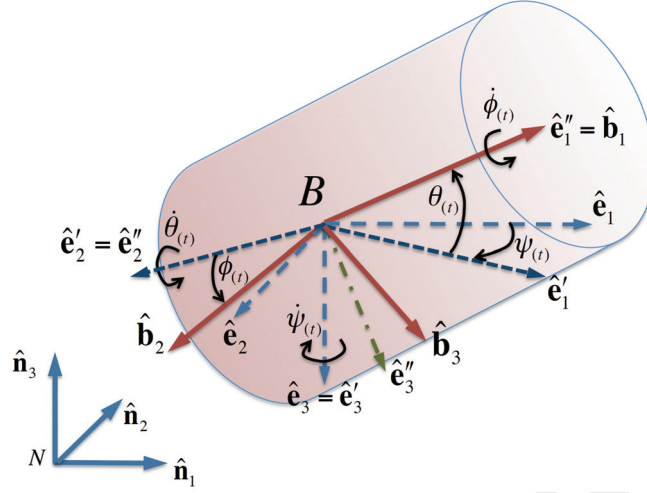
24

Figure A.1: Schematic of rotation in Euler angles.

particle. $[\mathbf{T}_{NB}]$ is the orthogonal transformation matrix from body-fixed reference frame $\mathcal{B}$ to inertial reference frame $\mathcal{N}$.

The transformation matrix $\mathbf{T}_{NB}$ can be expressed in the terms of Euler angles $[\phi, \theta, \psi]^T$,

$$\mathbf{T}_{NB} = \begin{bmatrix} c\psi c\theta & c\psi s\phi s\theta - c\phi s\psi & s\phi s\psi + c\phi c\psi s\theta \\ -s\psi c\theta & -s\psi s\phi s\theta - c\phi c\psi & s\phi c\psi - c\phi s\psi s\theta \\ s\theta & -s\phi c\theta & -c\phi c\theta \end{bmatrix}, \tag{A.2}$$

where c and s are short for cos and sin, respectively. The Euler angles $[\phi, \theta, \psi]^T$ are defined by the following rotation sequence,

1. Rotation of π radians respect to $\hat{\mathbf{n}}_1$ from frame $\mathcal{N}(\hat{\mathbf{n}}_1, \hat{\mathbf{n}}_2, \hat{\mathbf{n}}_3)$ to $\mathcal{E}(\hat{\mathbf{e}}_1, \hat{\mathbf{e}}_2, \hat{\mathbf{e}}_3)$, as shown in figure A.1
2. Rotation of ψ radians respect to $\hat{\mathbf{e}}_3$ from frame $\mathcal{E}(\hat{\mathbf{e}}_1, \hat{\mathbf{e}}_2, \hat{\mathbf{e}}_3)$ to $\mathcal{E}'(\hat{\mathbf{e}}_1', \hat{\mathbf{e}}_2', \hat{\mathbf{e}}_3')$
3. Rotation of θ radians respect to $\hat{\mathbf{e}}_2'$ from frame $\mathcal{E}'(\hat{\mathbf{e}}_1', \hat{\mathbf{e}}_2', \hat{\mathbf{e}}_3')$ to $\mathcal{E}''(\hat{\mathbf{e}}_1'', \hat{\mathbf{e}}_2'', \hat{\mathbf{e}}_3'')$
4. Rotation of ϕ radians respect to $\hat{\mathbf{e}}_1''$ from frame $\mathcal{E}''(\hat{\mathbf{e}}_1'', \hat{\mathbf{e}}_2'', \hat{\mathbf{e}}_3'')$ to $\mathcal{B}(\hat{\mathbf{b}}_1, \hat{\mathbf{b}}_2, \hat{\mathbf{b}}_3)$.

The angular velocity of body-fixed frame $\mathcal{B}$ with respect to the inertial frame $\mathcal{N}$ can be expressed in terms of the time derivatives of the Euler angles,

$$\omega_E^B = \dot{\psi}\hat{\mathbf{e}}_3 + \dot{\theta}\hat{\mathbf{e}}_2' + \dot{\phi}\hat{\mathbf{e}}_1''. \tag{A.3}$$

Eq. (A.3) can be expressed in the terms of unit vectors $(\hat{\mathbf{n}}_1, \hat{\mathbf{n}}_2, \hat{\mathbf{n}}_3)$ in frame $\mathcal{N}$,

$$\omega_N^B = \begin{bmatrix} \cos\theta\cos\psi & -\sin\psi & 0 \\ -\cos\theta\sin\psi & -\cos\psi & 0 \\ \sin\theta & 0 & -1 \end{bmatrix} \begin{pmatrix} \dot{\phi} \\ \dot{\theta} \\ \dot{\psi} \end{pmatrix} \triangleq [\mathbf{B}]\dot{\phi}^B, \tag{A.4}$$

where $\dot{\phi}^B = [\dot{\phi}\ \dot{\theta}\ \dot{\psi}]^T$ is the vector of Euler angle time derivatives, and $[\mathbf{B}]$ the coefficient matrix. The corresponding angular acceleration is given by

$$\alpha_N^B = \dot{\omega}_N^B = [\mathbf{B}]\ddot{\phi}^B + [\dot{\mathbf{B}}]\dot{\phi}^B. \tag{A.5}$$

For the frame $\mathcal{B}$ fixed on the Sth solid body, we have $\omega_N^B = \mathbf{\Omega}_N^S$ and $\alpha_N^B = \dot{\mathbf{\Omega}}_N^S$. The velocity and acceleration of a point P on the Sth solid body are

$$\mathbf{V}_N^P = \mathbf{V}_N^S + \mathbf{\Omega}_N^S \times \left([\mathbf{T}_{NB}]\mathbf{R}_B^P\right), \tag{A.6}$$

$$\dot{\mathbf{V}}_N^P = \dot{\mathbf{V}}_N^S + \dot{\mathbf{\Omega}}_N^S \times \left([\mathbf{T}_{NB}]\mathbf{R}_B^P\right) + \mathbf{\Omega}_N^S \times \mathbf{\Omega}_N^S \times \left([\mathbf{T}_{NB}]\mathbf{R}_B^P\right), \tag{A.7}$$

where $\mathbf{V}_N^S = \dot{\mathbf{R}}_N^S$ is the translational velocity of the frame $\mathcal{B}$ fixed on the Sth solid body.

25

Appendix A.2. Dynamics

The origin of the body-fixed frame $\mathcal{B}$ in this work is at the center of mass. For the Sth rigid body, the Newton-Euler equations of motion can be given by

$$
\begin{align}
\dot{\mathbf{R}}_N^S &= \mathbf{V}_N^S, \tag{A.8}\\
[\mathbf{M}_S]\,\dot{\mathbf{V}}_N^S &= \mathbf{F}_N^S, \tag{A.9}\\
[\mathbf{B}]\,\dot{\phi}^B &= \omega_N^B, \tag{A.10}\\
[\mathbf{I}_N]\,\dot{\omega}_N^B &= \mathbf{M}_N^S - \omega_N^B \times \left([\mathbf{I}_N]\,\omega_N^B\right), \tag{A.11}
\end{align}
$$

where $\mathbf{F}_N^S$ is the external force acting on the Sth solid body. $\mathbf{M}_N^S$ is the resultant moment of external forces respect to the Sth rigid body's center of mass. $[\mathbf{M}_S] = diag(m_S)_{3\times3}$ is the mass matrix, where m_S is the mass of the Sth solid body. $[\mathbf{I}_N] = [\mathbf{T}_{NB}][\mathbf{I}_B][\mathbf{T}_{NB}]^T$ is the inertia matrix in the inertial frame $\mathcal{N}$, and $[\mathbf{I}_B]$ is the inertia matrix around the axes of the body-fixed frame $\mathcal{B}$.

In order to be able to use general time integration schemes, the equations are re-casted by using the generalized displacement and velocity as follows

$$
\begin{align}
\mathbf{s}(t) &= \left[\mathbf{R}_N^S \ \phi^B \ \gamma^B\right]^T \tag{A.12}\\
\mathbf{u}(t) &= \left[\dot{\mathbf{R}}_N^S \ \dot{\phi}^B \ \dot{\gamma}^B\right]^T, \tag{A.13}
\end{align}
$$

where $\phi^B = [\phi \ \theta \ \psi]^T$ is the angle vector in the form of Euler angles. γ^B is defined by

$$
\gamma^B = \int_{t_0}^t \omega_N^B dt \tag{A.14}
$$

with $\gamma_B(t_0) = 0$.

The reordered equations of motion are

$$
\begin{align}
[\mathbf{M}_{ES}]_{9\times9}\,\dot{\mathbf{s}} &= [\mathbf{G}]_{9\times9}\,\mathbf{u} \tag{A.15}\\
[\mathbf{M}_{EU}]_{9\times9}\,\dot{\mathbf{u}} &= \mathbf{R}_E, \tag{A.16}
\end{align}
$$

where

$$
[\mathbf{M}_{ES}]_{9\times9} = \left[\begin{array}{ccc} [\mathbf{I}]_{3\times3} & [0]_{3\times3} & [0]_{3\times3} \\ [0]_{3\times3} & [\mathbf{B}]_{3\times3} & [0]_{3\times3} \\ [0]_{3\times3} & [0]_{3\times3} & [\mathbf{I}]_{3\times3} \end{array}\right], \tag{A.17}
$$

$$
[\mathbf{M}_{EU}]_{9\times9} = \left[\begin{array}{ccc} [\mathbf{M}_S]_{3\times3} & [0]_{3\times3} & [0]_{3\times3} \\ [0]_{3\times3} & [\mathbf{B}]_{3\times3} & -[\mathbf{I}]_{3\times3} \\ [0]_{3\times3} & [0]_{3\times3} & [\mathbf{I}_N]_{3\times3} \end{array}\right], \tag{A.18}
$$

$$
[\mathbf{G}]_{9\times9} = \left[\begin{array}{ccc} [\mathbf{I}]_{3\times3} & [0]_{3\times3} & [0]_{3\times3} \\ [0]_{3\times3} & [0]_{3\times3} & [\mathbf{I}]_{3\times3} \\ [0]_{3\times3} & [0]_{3\times3} & [\mathbf{I}]_{3\times3} \end{array}\right], \tag{A.19}
$$

$$
[\mathbf{R}_E] = \left[\begin{array}{c} \mathbf{F}_N^S \\ -\left[\dot{\mathbf{B}}\right]\phi^B \\ \mathbf{M}_N^S - \omega_N^B \times \left([\mathbf{I}_N]\,\omega_N^B\right) \end{array}\right]. \tag{A.20}
$$

Here, $\mathbf{I}$ is the identity matrix. In Eq. (A.16), the equation for $\ddot{\phi}_B$ was obtained from Eq. (A.5). Although analytically the equations for $\dot{\phi}^B$ and $\ddot{\phi}^B$ are redundant (one is obtained from taking the time derivative of the other), the matrices $[\mathbf{M}]_{ES}$ and $[\mathbf{G}]$ are defined such that the constraint on $\dot{\phi}_B$ given by Eq. (A.4) is enforced exactly. Then, for a given discrete time integration algorithm, the vector $\dot{\phi}_B$ can be evolved from $\ddot{\phi}_B$ using the scheme, and then modified to satisfy the constraint Eq. (A.5) for each time iteration/sub-iteration step.

For a solid body moving in two dimensional space, the equations of motion (A.15) and (A.16) can be significantly simplified. For example, the transformation matrix $\mathbf{T}_{NB}$ for a rigid body moving in the space defined by the $\hat{\mathbf{n}}_1$ and $\hat{\mathbf{n}}_2$ reduces to the following form, by setting $\phi = \theta = 0$

$$\mathbf{T}_{NB} = \begin{bmatrix} \cos\psi & -\sin\psi & 0 \\ -\sin\psi & -\cos\psi & 0 \\ 0 & 0 & -1 \end{bmatrix}. \tag{A.21}$$

The angular velocity vector $\dot{\phi}^B$ reduces to $\dot{\phi}^B = [0 \; 0 \; \dot{\psi}]^T$, and we can get $\omega_N^B = -\dot{\phi}^B$.

References

[1] A. Prosperetti, G. Tryggvason, Computational methods for multiphase flow, Cambridge University Press, Chapter 1, 2007.

[2] M. Bourgoin, H. Xu, Focus on dynamics of particles in turbulence, New Journal of Physics 16 (8) (2014) 085010.

[3] A. Guha, Transport and deposition of particles in turbulent and laminar flow, Annual Review of Fluid Mechanics 40 (2008) 311–341.

[4] S. Tenneti, S. Subramaniam, Particle-resolved direct numerical simulation for gas-solid flow model development, Annual Review of Fluid Mechanics 46 (2014) 199–230.

[5] A. Ferrante, S. Elghobashi, On the physical mechanisms of two-way coupling in particle-laden isotropic turbulence, Physics of Fluids 15 (2) (2003) 315–329.

[6] L. P. Wang, B. Rosa, H. Gao, G. He, G. Jin, Turbulent collision of inertial particles: point-particle based, hybrid simulations and beyond, International Journal of Multiphase Flow 35 (9) (2009) 854–867.

[7] G. Jin, G. W. He, L. P. Wang, Large-eddy simulation of turbulent collision of heavy particles in isotropic turbulence, Physics of Fluids 22 (5) (2010) 055106.

[8] H. H. Hu, N. A. Patankar, M. Zhu, Direct numerical simulations of fluid–solid systems using the arbitrary Lagrangian–Eulerian technique, Journal of Computational Physics 169 (2) (2001) 427–462.

[9] D. Qi, Lattice-Boltzmann simulations of fluidization of rectangular particles, International Journal of Multiphase Flow 26 (3) (2000) 421–433.

[10] A. Ladd, R. Verberg, Lattice-Boltzmann simulations of particle-fluid suspensions, Journal of Statistical Physics 104 (5-6) (2001) 1191–1251.

[11] Z. G. Feng, E. E. Michaelides, The immersed boundary-lattice Boltzmann method for solving fluid–particles interaction problems, Journal of Computational Physics 195 (2) (2004) 602–628.

[12] R. Glowinski, T.-W. Pan, T. I. Hesla, D. D. Joseph, A distributed Lagrange multiplier/fictitious domain method for particulate flows, International Journal of Multiphase Flow 25 (5) (1999) 755–794.

[13] N. A. Patankar, P. Singh, D. D. Joseph, R. Glowinski, T.-W. Pan, A new formulation of the distributed Lagrange multiplier/fictitious domain method for particulate flows, International Journal of Multiphase Flow 26 (9) (2000) 1509–1524.

[14] N. Sharma, N. A. Patankar, A fast computation technique for the direct numerical simulation of rigid particulate flows, Journal of Computational Physics 205 (2) (2005) 439–457.

[15] Z. Yu, X. Shao, Direct numerical simulation of particulate flows with a fictitious domain method, International Journal of Multiphase Flow 36 (2) (2010) 127–134.

[16] A. Wachs, PeliGRIFF, a parallel DEM-DLM/FD direct numerical simulation tool for 3D particulate flows, Journal of Engineering Mathematics 71 (1) (2011) 131–155.

[17] C. S. Peskin, Flow patterns around heart valves: a numerical method, Journal of Computational Physics 10 (2) (1972) 252–271.

[18] E. Fadlun, R. Verzicco, P. Orlandi, J. Mohd-Yusof, Combined immersed-boundary finite-difference methods for three-dimensional complex flow simulations, Journal of Computational Physics 161 (1) (2000) 35–60.

[19] M. Uhlmann, An immersed boundary method with direct forcing for the simulation of particulate flows, Journal of Computational Physics 209 (2) (2005) 448–476.

[20] Z. Zhang, A. Prosperetti, A second-order method for three-dimensional particle simulation, Journal of Computational Physics 210 (1) (2005) 292–324.

[21] T. Kempe, J. Fröhlich, An improved immersed boundary method with direct forcing for the simulation of particle laden flows, Journal of Computational Physics 231 (9) (2012) 3663–3684.

[22] S. Haeri, J. Shrimpton, On the application of immersed boundary, fictitious domain and body-conformal mesh methods to many particle multiphase flows, International Journal of Multiphase Flow 40 (2012) 38–55.

[23] R. Mittal, G. Iaccarino, Immersed boundary methods, Annual Review of Fluid Mechanics 37 (2005) 239–261.

[24] K. Luo, Z. Wang, J. Fan, K. Cen, Full-scale solutions to particle-laden flows: Multidirect forcing and immersed boundary method, Physical Review E 76 (6) (2007) 066709.

[25] M. Vanella, E. Balaras, A moving-least-squares reconstruction for embedded-boundary formulations, Journal of Computational Physics 228 (18) (2009) 6617–6628.

[26] A. Pinelli, I. Z. Naqavi, U. Piomelli, J. Favier, Immersed-boundary methods for general finite-difference and finite-volume Navier-Stokes solvers, J. Comput. Phys. 229 (24) (2010) 9073–9091.

[27] S. Wang, X. Zhang, An immersed boundary method based on discrete stream function formulation for two-and three-dimensional incompressible flows, Journal of Computational Physics 230 (9) (2011) 3479–3499.

[28] X. Yang, X. Zhang, Z. Li, G. W. He, A smoothing technique for discrete delta functions with application to immersed boundary method in moving boundary simulations, Journal of Computational Physics 228 (20) (2009) 7821–7836.

[29] F. Lucci, A. Ferrante, S. Elghobashi, Modulation of isotropic turbulence by particles of Taylor length-scale size, Journal of Fluid Mechanics 650 (2010) 5–55.

27

[30] M. Uhlmann, Interface-resolved direct numerical simulation of vertical particulate channel flow in the turbulent regime, Physics of Fluids 20 (5) (2008) 053305.

[31] M. Garcia-Villalba, A. G. Kidanemariam, M. Uhlmann, DNS of vertical plane channel flow with finite-size particles: Voronoi analysis, acceleration statistics and particle-conditioned averaging, International Journal of Multiphase Flow 46 (2012) 54–74.

[32] A. G. Kidanemariam, C. Chan-Braun, T. Doychev, M. Uhlmann, Direct numerical simulation of horizontal open channel flow with finite-size, heavy particles at low solid volume fraction, New Journal of Physics 15 (2) (2013) 025031.

[33] B. Vowinckel, T. Kempe, J. Fröhlich, Fluid–particle interaction in turbulent open channel flow with fully-resolved mobile beds, Advances in Water Resources 72 (2014) 32–44.

[34] T. Kempe, B. Vowinckel, J. Fröhlich, On the relevance of collision modeling for interface-resolving simulations of sediment transport in open channel flow, International Journal of Multiphase Flow 58 (2014) 214–235.

[35] Y. Xu, S. Subramaniam, Effect of particle clusters on carrier flow turbulence: A direct numerical simulation study, Flow, Turbulence and Combustion 85 (3-4) (2010) 735–761.

[36] L. Botto, A. Prosperetti, A fully resolved numerical simulation of turbulent flow past one or several spherical particles, Physics of Fluids 24 (1) (2012) 013303.

[37] E. Balaras, C. Benocci, U. Piomelli, Two-layer approximate boundary conditions for large-eddy simulations, AIAA Journal 34 (6) (1996) 1111–1119.

[38] S. Armfield, R. Street, An analysis and comparison of the time accuracy of fractional-step methods for the Navier-Stokes equations on staggered grids, International Journal for Numerical Methods in Fluids 38 (3) (2002) 255–282.

[39] A. Posa, M. Vanella, E. Balaras, An adaptive reconstruction for Lagrangian, direct-forcing, immersed-boundary methods, J. Comput. Phys. 351 (2017) 422–436.

[40] H. Baruh, Analytical dynamics, WCB/McGraw-Hill Boston, 1999.

[41] J. Yang, S. Preidikman, E. Balaras, A strongly coupled, embedded-boundary method for fluid–structure interactions of elastically mounted rigid bodies, Journal of Fluids and Structures 24 (2) (2008) 167–182.

[42] J. Yang, E. Balaras, An embedded-boundary formulation for large-eddy simulation of turbulent flows interacting with moving boundaries, Journal of Computational Physics 215 (1) (2006) 12–40.

[43] T.-W. Pan, D. Joseph, R. Bai, R. Glowinski, V. Sarin, Fluidization of 1204 spheres: simulation and experiment, Journal of Fluid Mechanics 451 (2002) 169–191.

[44] M. Rahmani, A. Wachs, Free falling and rising of spherical and angular particles, Physics of Fluids 26 (8) (2014) 083301.

[45] M. Uhlmann, J. Dušek, The motion of a single heavy sphere in ambient fluid: a benchmark for interface-resolved particulate flow simulations with significant relative velocities, International Journal of Multiphase Flow 59 (2014) 221–243.

[46] A. Posa, E. Balaras, Model-based near-wall reconstructions for immersed-boundary methods, Theoretical and Computational Fluid Dynamics 28 (4) (2014) 473–483.

[47] D. Wan, S. Turek, An efficient multigrid-FEM method for the simulation of solid-liquid two phase flows, Journal of Computational and Applied Mathematics 203 (2) (2007) 561–580.

[48] S. Tenneti, R. Garg, S. Subramaniam, Drag law for monodisperse gas–solid systems using particle-resolved direct numerical simulation of flow past fixed assemblies of spheres, Int. J. Multiphas. Flow 37 (9) (2011) 1072–1092.

[49] M. Braza, P. Chassaing, H. H. Minh, Numerical study and physical analysis of the pressure and velocity fields in the near wake of a circular cylinder, Journal of Fluid Mechanics 165 (1986) 79–130.

[50] M. Coutanceau, R. Bouard, Experimental determination of the main features of the viscous flow in the wake of a circular cylinder in uniform translation. part 1. steady flow, Journal of Fluid Mechanics 79 (02) (1977) 231–256.

[51] M. N. Linnick, H. F. Fasel, A high-order immersed interface method for simulating unsteady incompressible flows on irregular domains, Journal of Computational Physics 204 (1) (2005) 157–192.

[52] K. Taira, T. Colonius, The immersed boundary method: A projection approach, Journal of Computational Physics 225 (2) (2007) 2118–2137.

[53] E. Guilmineau, P. Queutey, A numerical simulation of vortex shedding from an oscillating circular cylinder, Journal of Fluids and Structures 16 (6) (2002) 773–794.

[54] A. ten Cate, C. H. Nieuwstad, J. J. Derksen, H. E. A. Van den Akker, Particle imaging velocimetry experiments and lattice-Boltzmann simulations on a single sphere settling under gravity, Physics of Fluids 14 (11) (2002) 4012.

[55] P. L. Carroll, G. Blanquart, A proposed modification to lundgren's physical space velocity forcing method for isotropic turbulence, Physics of Fluids 25 (10) (2013) 105114.

[56] G. Bellani, M. L. Byron, A. G. Collignon, C. R. Meyer, E. A. Variano, Shape effects on turbulent modulation by large nearly neutrally buoyant particles, Journal of Fluid Mechanics 712 (2012) 41–60.

[57] S. Pope, Turbulent Flows, Cambridge University Press, 2000.